TEKTONIKA

From a Continental Margin to an Alpine Dome: 4D Geodynamic Evolution of the Aar Massif

Ferdinando Musso Piantelli *[1,2], **Lukas Nibourel** [3], **Alfons Berger** [2], **Marco Herwegh** [2]

[1]Swiss Geological Survey, Federal Office of Topography swisstopo, Seftigenstrasse 264, 3084 Bern, Switzerland | [2]Institute of Geological Sciences, University of Bern, Baltzerstrasse 1+3, 3012 Bern, Switzerland | [3]Department of Earth and Planetary Sciences, ETH Zurich, Sonneggstrasse 5, 8092 Zürich, Switzerland

Abstract The inversion of crystalline basement units of former passive continental margins is a typical feature of late-stage collisional mountain belts. In this study, a new large-scale 3D geological model of the main lithostratigraphic and structural units of the Aar Massif was built to investigate how the 3D geometry of the passive margin and inherited extensional structures influenced the tectonic evolution during late-stage continent-continent collision. Cross-section restoration of such units and of metamorphic peak temperature data allowed us to reconstruct the 4D geodynamic evolution of the massif during the late-stage Alpine orogeny. Our results show that: (i) The Aar Massif results from the inversion of the unevenly stretched proximal zone of the passive European margin. (ii) 20% of the present-day structural relief of the massif is a legacy of the 3D architecture of the Permian to Mesozoic passive continental margin. Mesozoic rifting structures formed larger-scale basins separated by a central topographic high subdividing the Aar Massif into three SW-NE trending basement blocks. (iii) The inherited spatial variations in graben/basins geometry and associated sediment and crustal thickness variations caused an in-sequence, non-cylindrical exhumation of the Aar Massif, controlled by a dense network of reverse and thrust faults. This interplay between crustal dynamics and crustal inheritance resulted in the uplift and emplacement of the Aar Massif. The results of this study highlight the importance of integrating regional-scale 3D geological modelling in the analysis of complex geological systems, such as orogens. By enabling a comprehensive understanding of their 4D evolution and geodynamic processes, this methodology opens the door to a wide range of applications in tectonics, resource exploration, and hazard assessment.

Executive Editor:
Robin Lacassin
Associate Editor:
Chiara Montomoli
Technical Editor:
Mohamed Gouiza

Reviewers:
Salvatore Iaccarino
Philippe H. Leloup

Submitted:
5 March 2025
Accepted:
16 December 2025
Published:
3 February 2026

1 Introduction

The closure of suture zones owing to convergent plate movements leads to a transition from ocean-continent subduction to continent-continent collision (e.g., *Beaumont et al.*, 2000; *Bellahsen et al.*, 2014; *Lacombe and Mouthereau*, 2002; *Mohn et al.*, 2012). In this process, the former passive continental margin of the subducting lower plate is progressively integrated into the upper plate, first involving the distal margin and then the proximal margin (e.g., *Mouthereau et al.*, 2013). Numerous studies have shown that thick-skinned tectonics and the development of shear zones in the crystalline basement are typically observed during the advanced stages of continent-continent collision involving an increasingly thick and buoyant proximal continental margin (*Lacombe and Bellahsen*, 2016; *Muñoz*, 1992; *Boutoux et al.*, 2014, 2016; *Pfiffner*, 2006; *Rosenberg et al.*, 2015; *Granado and Ruh*, 2019, e.g.,). During the inversion of former passive continental margins (e.g., Taiwan: *Beyssac et al.*, 2007; Zagros: *Vergés et al.*, 2011; Western Alps: *Tricart*, 1984; *Bellanger et al.*, 2014; *Spitz et al.*, 2020), the evolution is influenced by factors such as pre-collision crustal geometry, crustal thickness, and the reactivation or inhibition of inherited structures (e.g., *Rosenberg and Kissling*, 2013; *Lafosse et al.*, 2016; *Herwegh et al.*, 2024; *Nibourel et al.*, 2021a; *Musso Piantelli et al.*, 2022). Such inversion-related exhumation processes occur on a large scale (hundreds of km^3) and display highly non-cylindrical geometries (*Nibourel et al.*, 2021b; *Yin*, 2006). The complexity of such geometric variations in the orogen-parallel direction cannot be captured using 2D methods alone. Regional-scale 3D geological modelling is a powerful tool that allows the resolution of such complex three-dimensional settings and is often the key to new insights into the evolution of orogens (*Mock et al.*, 2020; *Brisson et al.*, 2023; *Frings et al.*, 2023). When restoration is applied to the 3D model, it is possible to study the orogen in 4D, which improves the understanding of the complex tectonic evolution in mountain belts and its lateral variability.

Along the Western and Central European Alps, the External Crystalline Massifs (from southwest to northeast, the Argentera, Pelvoux, Grandes Rousses, Grand Châtelard, Belledonne, Aiguilles Rouges, Mont Blanc, Aar and Gotthard Massifs; *Schmid et al.*,

*✉ ferdinando.musso@unibe.ch

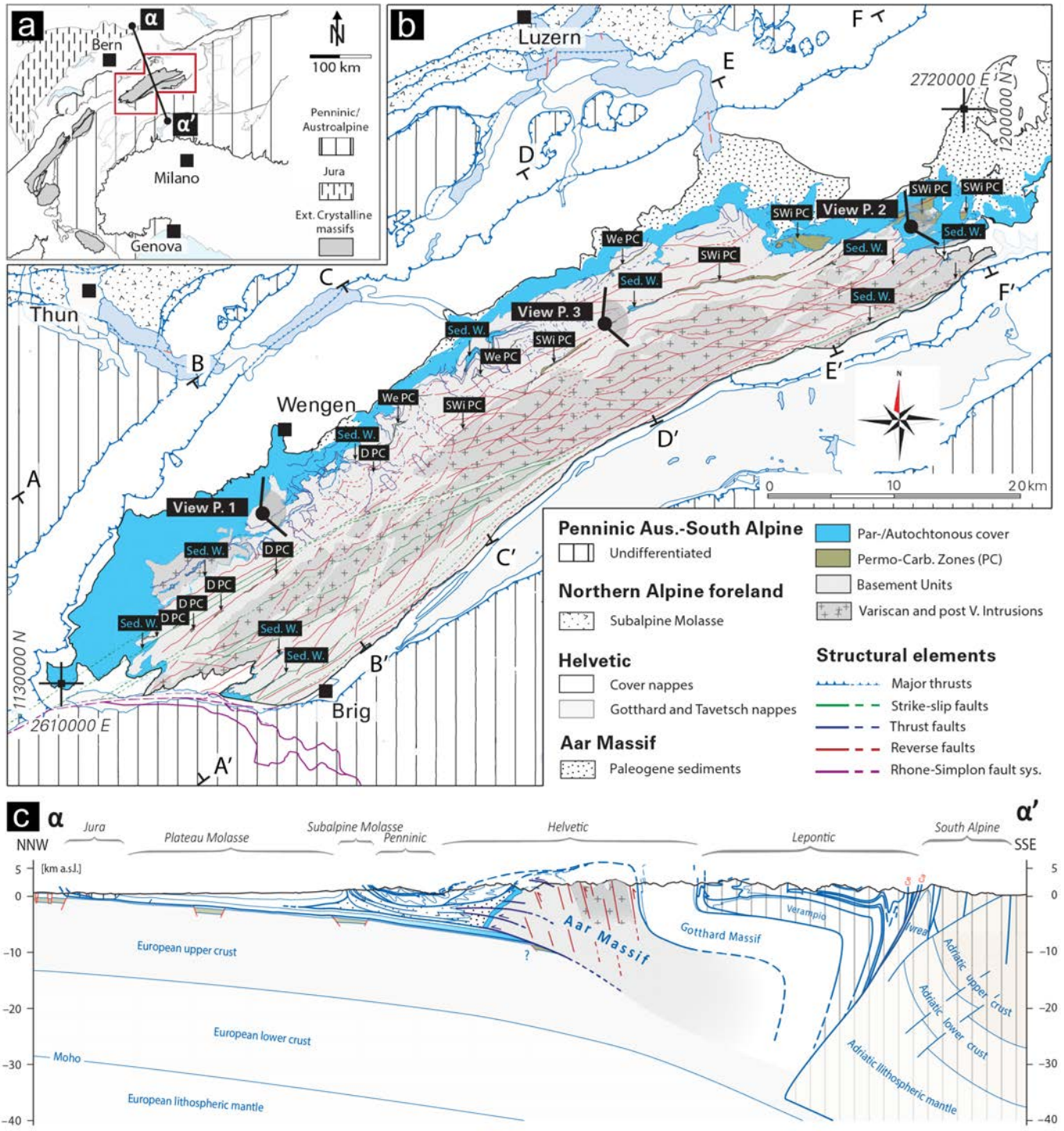

Figure 1 – Geological map and cross-section of the study area. (A) Regional overview map simplified after *Schmid et al.* (2004). (B) Geological map illustrating the large-scale trends of the main structural elements, the profile traces of Figure 2, the viewpoints of Figure 3, and the thin sediment wedges (Sed. W.) as well as the positions of the Susten-Windgälle (SWi PC), Doldenhorn (D PC) and Wenden (We PC) Permo-Carboniferous troughs. (C) Large-scale cross-section of the study area, modified after *swisstopo* (2024).

2004, Figure 1) are examples of antiformal complexes resulting from the inversion of the former European passive continental margin. These massifs form a laterally discontinuous belt of basement domes, which are separated by structural saddles (e.g., *Egli and Mancktelow*, 2013; *Granado and Ruh*, 2019; *Herwegh et al.*, 2024). A large number of field, structural, numerical and petrochronological studies have been conducted to understand the geodynamic processes leading to the formation of such basement domes (e.g., *Frey et al.*, 1980; *Burkhard*, 1988; *Herwegh and Pfiffner*, 2005; *Leloup et al.*, 2005; *Pfiffner*, 2006; *Bellahsen et al.*, 2012; *Boutoux et al.*, 2014; *Bauville and Schmalholz*, 2015, 2017; *Lacombe and Bellahsen*, 2016; *Granado and Ruh*, 2019; *Girault et al.*, 2020, 2022; *Herwegh et al.*, 2024). These previous approaches have documented and studied deformation structures in structural maps and/or on cross-sections, while the three-dimensional

and non-cylindrical architecture and evolution of these complexes remain largely unexplored, with only limited studies addressing these aspects (*Campani et al.*, 2014; *Musso Piantelli et al.*, 2022; *Mercier et al.*, 2023).

In this work, we selected the Aar Massif (Central European Alps; Figure 1), the easternmost of the External Crystalline Massifs, to examine how passive margin geometry, inherited structures and crustal thickness variations influenced the late stages of continent-continent collision. To visualise the three-dimensional architecture of the massif, we constructed a large-scale explicit 3D geological model of the main lithological and tectonic boundaries of the area.

By combining cross-section restoration, published metamorphic peak temperature data (*Nibourel et al.*, 2021b, and references therein), and a series of structural, geomorphological, thermochronological, and geochemical studies conducted in recent years (*Burkhard*, 1988; *Hänni and Pfiffner*, 2001; *Herwegh and Pfiffner*, 2005; *Pfiffner et al.*, 2011; *Berger et al.*, 2017a,b, 2020; *Wehrens et al.*, 2016, 2017; *Schneeberger et al.*, 2017; *Herwegh et al.*, 2017, 2020, 2024; *Mair et al.*, 2018; *Nibourel et al.*, 2018, 2021b,a; *Baumberger et al.*, 2022; *Musso Piantelli et al.*, 2022, 2023), we then built a 4D crustal geodynamic reconstruction of the evolution of the Aar Massif during the late stage of Alpine collision (22-0 Ma).

2 Geological Setting and Age Constraints

The Aar Massif is an east-northeast-trending structural half dome outcropping for more than 2000 km^2 at an average elevation of ~2200 m a.s.l. in the central Swiss Alps (Figure 1). The Aar Massif is the largest and easternmost of the External Crystalline Massifs (e.g., *Herwegh et al.*, 2024). It exposes the basement units of the thickened lower European plate as a result of the convergence with the Adriatic plate and the associated post-35 Ma continent-continent collision (e.g., *Froitzheim et al.*, 1996; *Pfiffner*, 2024; *Schmid et al.*, 1996, 2004).

The basement units consist predominantly of pre-Variscan polycyclic metamorphic gneisses, migmatites and amphibolites (*Abrecht*, 1994; *Berger et al.*, 2017a). These gneissic units were intruded by Variscan to post-Variscan plutons, mostly in the central regions of the massif where they outcrop over ~760 km^2 (Figures 1 and 2). The emplacement of these plutons was associated with the formation of Permo-Carboniferous half-graben structures in the upper crust, which were filled by volcanic-, volcanoclastic and sedimentary sequences. The overlying succession of limestone, marl, shale, and sandstone, composing the para/autochthonous sedimentary units, were deposited during the Mesozoic to Cenozoic. Part of the autochthonous sedimentary cover of the Aar Massif was tectonically detached from its substrate. These detached units, referred to as the parautochthonous cover, form a series of nappes or tectonic slices. They contain incomplete successions of the same stratigraphic units preserved in the autochthonous cover (see *Berger et al.*, 2017a) and are therefore described and discussed together in this contribution. The geometry of the margin and the sedimentation pattern were controlled by extensional Mesozoic faults, resulting in large thickness variations that can still be observed along the strike of the massif (Figure 2 *Günzler-Seiffert*, 1952; *Trümpy*, 1980; *Strasser*, 1982; *Burkhard*, 1988; *Cardello and Mancktelow*, 2014; *Pfiffner*, 2024; *Musso Piantelli et al.*, 2022). These thickness variations have been documented by several authors at multiple locations within the Aar Massif, commonly presented in the form of stratigraphic columns (*Krebs*, 1925; *Rohr*, 1926; *Collet*, 1947; *Masson et al.*, 1980; *Dolivo*, 1982; *Gisler et al.*, 2007; *Krayenbuhl and Steck*, 2009; *Ziegler and Isler*, 2013; *Mair et al.*, 2018). Importantly, these columns consistently document greater thicknesses to the western and eastern regions of the massif, and more limited thickness and stratigraphy in its central part (see *Musso Piantelli et al.*, 2022).

Along the strike of the massif, Permo-Carboniferous to Cenozoic sediments are also locally preserved in narrow WSW-ENE-trending steep wedges (Figures 1 and 3c; e.g., *Rohr*, 1926; *Herwegh et al.*, 2020; *Nibourel et al.*, 2021a). The occurrence of these wedges is aligned along specific intensely deformed gneiss boundaries traceable along the strike of the massif (see *Berger et al.*, 2017b). In this study, such zones have been named as follows: Susten-Windgälle, Doldenhorn, Wenden and Gastern Permo-Carboniferous troughs (Figures 1 and 2). The structural crustal discontinuities formed by these half-grabens often represent the sites of subsequent extension by normal faulting during Mesozoic rifting.

During the collisional stage, the Aar Massif experienced a protracted exhumation history from approximately 22 Ma to the present (*Herwegh et al.*, 2020), accompanied by the development of a dense network of Alpine faults. Metamorphic conditions during deformation varied significantly across the massif. At its northern rim, Alpine metamorphic temperatures did not exceed ~250°C (e.g., *Bambauer et al.*, 2009; *Berger et al.*, 2017b; *Herwegh et al.*, 2017; *Rosenberg et al.*, 2021). At the southern boundary, peak Alpine conditions reached approximately 450°C and 600 MPa, corresponding to upper greenschist facies (*Goncalves et al.*, 2012; *Herwegh et al.*, 2020). Under these conditions, the basement units were primarily deformed in a ductile manner, as evidenced by the formation of mylonites and ultramylonites. However, brittle precursors and episodes of rapid embrittlement also contributed to strain localization (*Wehrens et al.*, 2016, 2017). This deformation resulted in a dense network of subvertical to steeply inclined shear zones that dissect the Aar Massif (see *Baumberger et al.*, 2022, and references therein).

With progressive deformation and exhumation, the basement rocks reached shallower crustal levels and lower temperatures. During this stage, brittle deformation often reactivated pre-existing ductile structures. This led to the formation of brittle fractures, cataclasites,

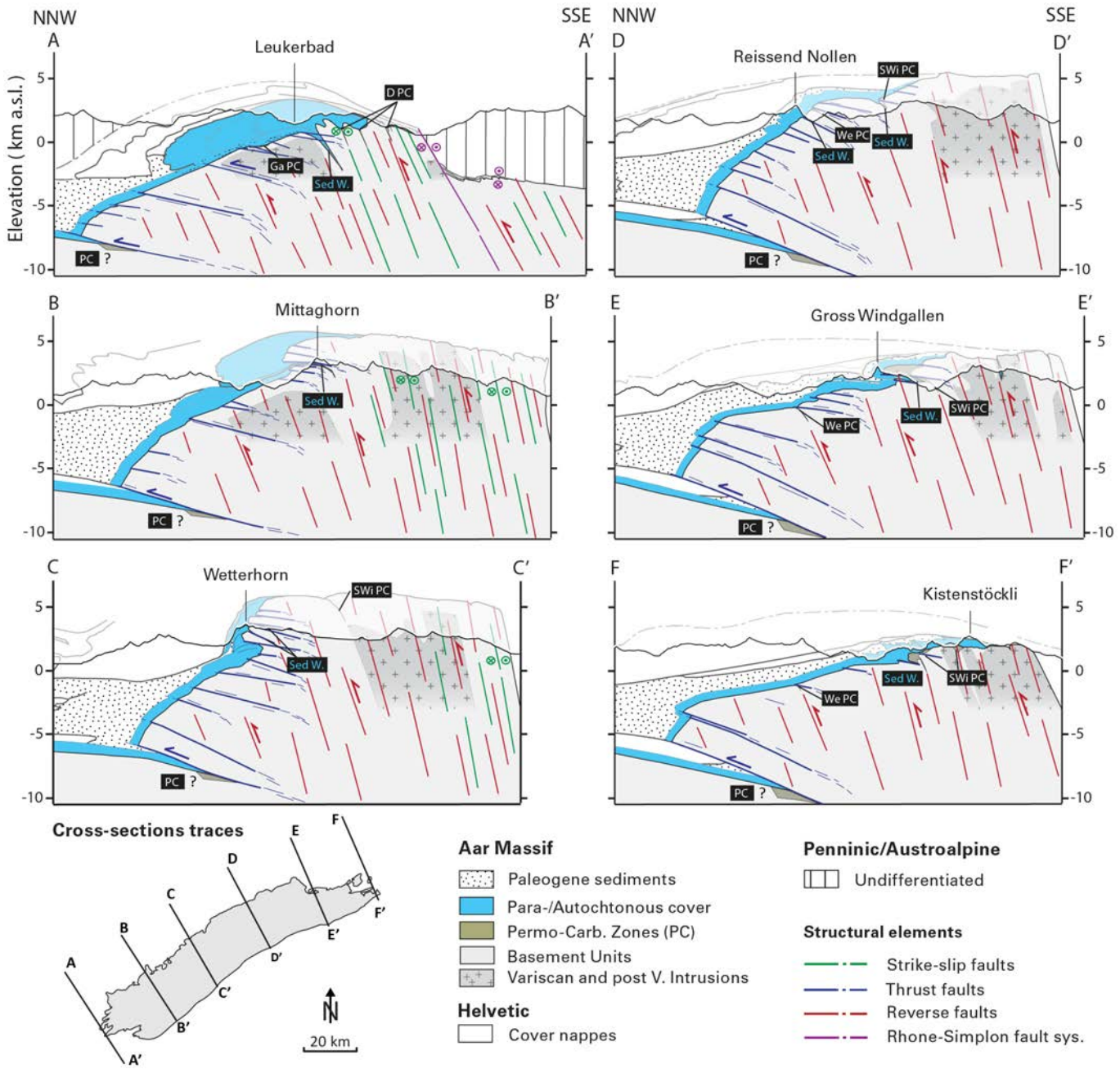

Figure 2 – Cross-sections of the study area. The profiles show main structural elements, the overlying Helvetic, Penninic and Austroalpine nappes and the Susten-Windgälle (SWi PC), Doldenhorn (D PC), Wenden (We PC) and Gastern (Ga PC) Permo-Carboniferous troughs as well as several sedimentary wedges (Sed W.). Reverse faults are shown using a patterned style due to their high frequency and dense distribution. In sections AA', BB' and CC' the outline of the overlying upper Helvetic nappes has been modified after *Herwegh and Pfiffner* (2005), *Hänni and Pfiffner* (2001), and *Musso Piantelli et al.* (2022). The sections highlight the half dome-shape of the crystalline units of the massif, which reaches an elevation of 6 km a.s.l. in the central regions (CC') and loses elevation on the sides (AA' and FF'). Furthermore, along the strike of the massif, significant changes in the thickness of the Para/Autochthonous sedimentary cover can be observed.

fault gouges, and breccias. As a result, individual structural discontinuities often exhibit both ductile and brittle deformation characteristics, behaving as shear zones at depth and as faults at shallower levels, with a brittle–ductile transition in between. To aid in clear and consistent communication, we refer to these structures collectively as "faults" throughout this contribution, following the nomenclature of *Sibson* (1977).

The kinematics and the age of these faults have been investigated and described in many scientific publications over the past decades (see *Herwegh et al.*, 2017, 2020; *Niboureel et al.*, 2021a, and references therein). In this study, we largely rely on such literature for the kinematics and age of the faults. A summary per fault type is provided below, but the reader is encouraged to consult the cited literature for more details.

2.1 Reverse Faults

Between 22 Ma and 12 Ma steep to sub-vertical NW-SE striking reverse faults formed within the massif, contributing to its exhumation (e.g., Handegg phase;

Steck, 1968; *Wehrens et al.*, 2017; *Bergemann et al.*, 2017; *Herwegh et al.*, 2017, 2020; *Mair et al.*, 2018; *Nibourel et al.*, 2021a). Kinematic indicators at both outcrop and microscale predominantly show south-block-up motion along these faults. Although individual fault planes accommodate only small displacements (few tens of metres or often less), their cumulative effect produces significant differential uplift at the regional scale. This is well observable where steep basement reverse faults locally steepen the originally shallow-dipping basement–cover contact (e.g., Figure 3c). Because these small offsets are distributed across many faults, they cannot be shown individually at map or cross-section scale (1:25,000). Consequently, Figure 4 includes only the most prominent structures. In cross-sections and field images of this work, a pattern style was used to depict the overall trend and orientation of these reverse faults. In the southern regions of the Aar Massif, these reverse faults have been dated to start around 22-20 Ma and were active till about 14-12 Ma, as dated on the base of isotopic Rb/Sr and Ar/Ar ages on micas (*Berger et al.*, 2017a; *Challandes et al.*, 2008; *Rolland et al.*, 2009) as well as monazites and adularia from associated clefts (*Bergemann et al.*, 2017; *Ricchi et al.*, 2019). During this reverse faulting a peak metamorphic gradient from 450°C to 250° evolved from S to N indicating differential uplift during progressive in-sequence northward propagation of new reverse faults. The time-integrated lateral migration of the reverse faults in space and time led to the passive "up-doming" of the overlaying sedimentary cover of the massif and Helvetic and Penninic nappe stack (Figure 2; e.g., Handegg faults; *Mock*, 2014; *Wehrens et al.*, 2017; *Herwegh et al.*, 2020; *Nibourel et al.*, 2021a,b).

2.2 Thrust Faults

In the Aar Massif, two main stages of thrusting have been documented, which are separated both temporally and spatially: (a) early and (b) late thrusts. The previously described reverse faults passively rotate and overprint the early thrusts, but are cut by the late thrusts, providing robust relative age constraints for the deformation sequence: early thrusts, reverse faults, late thrusts (see *Nibourel et al.*, 2021a,b, and references therein). Offsets along the basement-cover contact or slickenlines on these thrust surfaces consistently indicate top-to-the-NNW kinematics (e.g., early thrusts = see D2 thrusts; *Nibourel et al.*, 2021a,b, and references therein; late thrusts = Pfaffenchopf faults; *Mock*, 2014; *Wehrens et al.*, 2017; *Herwegh et al.*, 2020, and references therein).

(a) Early thrusts are currently exposed at the highest elevations formed at a transitional stage between latest Helvetic nappe stacking and at the early stages of massif exhumation. This is documented by field measurements and cross-sections of *Nibourel et al.* (2021a) and references therein, showing early thrusts (D2; *Nibourel et al.*, 2021a) being overprinted and rotated by subsequent steep to sub-vertical reverse faults (D3; *Nibourel et al.*, 2021a). The timing of this phase of early thrusting is poorly constrained by zircon fission track ages and (U-Th)/He ages on zircon between 27 and 19 Ma along the northern Aar Massif (*Michalski and Soom*, 1990; *Nibourel et al.*, 2018).

(b) Today, late thrusts are exposed at the northernmost regions of the Aar Massif. In the northern Hasli Valley, zircon fission-track ages (*Herwegh et al.*, 2020) date a major late-thrust system to ~12 Ma, post-dating the reverse faults described above. Based on interpretations of NFP20 seismic profiles and P-wave tomography (*Pfiffner et al.*, 1997; *Diehl et al.*, 2021), additional late-thrust systems were inferred by *Herwegh et al.* (2020, 2024) to occur at depth. From a geodynamic perspective, these systems were active between ~12 and 5 Ma, accommodated large offsets (up to several kilometres), and produced an "en bloc" staged exhumation of the massif (*Herwegh et al.*, 2020, 2024; *Nibourel et al.*, 2021a,b). These structures therefore formed sequentially, from the highest presently exposed thrusts down to the lowermost thrusts at the base of the massif (e.g., *Herwegh et al.*, 2020, 2024; *Nibourel et al.*, 2021a,b).

2.3 Dextral Strike-slip and Back Thrust Faults

Synchronous with the "en bloc" exhumation of the massif, shortening combined with dextral shearing affected the southern rim of the Aar Massif. In the south-eastern Aar Massif, widely spaced south-vergent back-thrust faults, ranging from a few tens to a few hundred meters in length, developed (*Nibourel et al.*, 2021a,b). Because of their limited size, these back-thrusts cannot be displayed or resolved in the regional-scale 3D model of the Aar Massif. Their occurrence becomes increasingly rare toward the central part of the massif.

This deformation phase is instead dominated by pronounced crustal-scale dextral strike-slip faults, most notably the Grimsel shear zone system (Figure 1; Oberaar phase: *Wehrens et al.*, 2017; *Herwegh et al.*, 2020, 2024). The age of these faults is constrained by isotopic ages on syn-kinematic white mica and biotite from cross-cutting strike-slip faults (*Challandes et al.*, 2008; *Rolland et al.*, 2009) and monazites in structurally controlled clefts (*Bergemann et al.*, 2017; *Ricchi et al.*, 2019). From a geodynamic perspective, dextral shearing in the Aar Massif is both kinematically and temporally linked to activity along the Simplon normal fault, which operated between ~18 and 5 Ma (e.g., *Campani et al.*, 2012, 2014; *Wolff et al.*, 2024). Above the low-angle Simplon fault, the hanging wall underwent SW-directed stretching and transport (e.g., *Mancktelow*, 1985). This extensional regime is decoupled north of the Rhone Line, which forms a steep lateral boundary accommodating dextral strike-slip motion (Figure 2; *Grosjean et al.*, 2004; *Campani et al.*, 2014). This dextral kinematic framework correlates with the Oberaar-phase shearing in the Aar Massif.

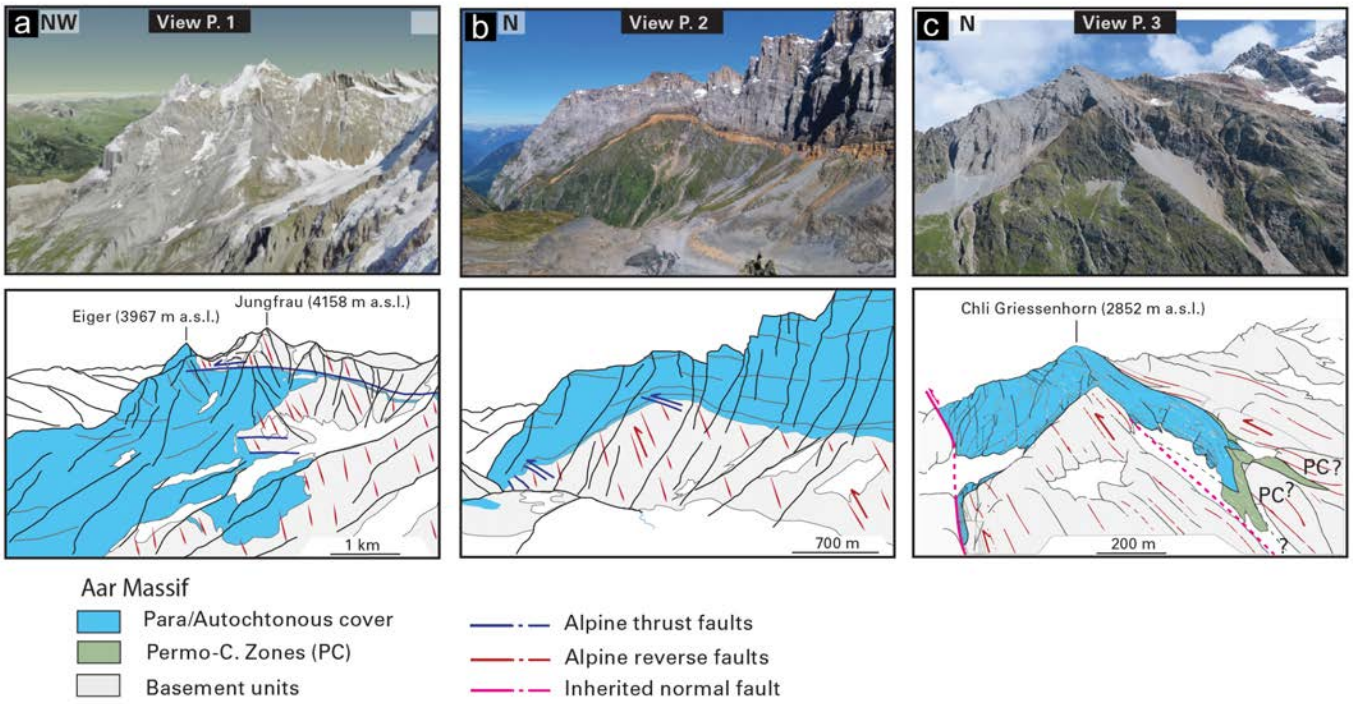

Figure 3 – Profile-like view of three type localities of the Aar Massif; viewpoints are indicated in Figure 1, and coordinates in the Supporting Information. Reverse faults are shown using a patterned style due to their high frequency and dense distribution. **(A)** Eiger-Mönch-Jungfrau complex. One of the structurally highest large-scale thrust dissects the basement units and pushes a rigid basement slab into the sedimentary cover. The main thrust plane is bent and dips to the NW. **(B)** Sedimentary cover-basement contact. The basement units are dissected by several reverse faults and small-scale thrust faults. At the northern front, the basement-cover contact dips steeply to the NW. **(C)** Färnigen zone (modified after *Nibourel et al.*, 2021a). The zone comprises two synformal sediment wedges, bounded by two early Jurassic normal faults (purple), and associated Permo-Carboniferous sediments. The original half-graben geometry, as well as the inherited normal fault, are still recognizable and preserved in the field. Field data from *Nibourel et al.* (2021a) indicate that the normal faults were only weakly reactivated during Alpine inversion.

3 Methods

3.1 Geological Data Compilation, Establishment of a Stratigraphic Model and Fieldwork

A detailed geological and structural map of the massif was produced, mapping the major stratigraphic and tectonic boundaries of both the sedimentary cover and basement units (see Supporting Information and Figure 4). Faults were identified remotely at a scale of 1:25 000 using high-resolution orthophotos (SwissImage, raster resolution 0.25 × 0.25 m; swisstopo), a high-resolution Digital Elevation Model (swissALTI3D, downsampled raster resolution 2 × 2 m, version 2013; swisstopo), and derived hillshade maps. The accuracy of remote fault detection was assessed at multiple scales by integrating UAV imagery and subsequent field verification at several sites, which showed a high correspondence (see *Baumberger et al.*, 2022; *Musso Piantelli et al.*, 2023). The geological map was further validated at key field locations through detailed mapping and structural data collection (see *Musso Piantelli et al.*, 2022). The geometry of the structures was characterised by more than 2500 field measurements (fault planes, dip direction/dip, and stretching lineation/slickenlines, of which over 1000 were collected in this study and the rest compiled from *Baumberger et al.*, 2022; *Wehrens et al.*, 2016; *Mair et al.*, 2018; *Nibourel et al.*, 2021b) and by the generation of rose plots. These were based on the remotely sensed lineament maps and calculated using a line-bearing Python algorithm (Line direction histogram).

3.2 3D Explicit Geological Modelling

All available data (mapped boundaries and structures, strike and dip data, tunnels and seismic sections) were imported into the software Move™ (Petex, v.2019.1) and projected onto a DEM (raster resolution 35x35 m). Here, a dense regularly spaced (500 m) network of NNW-SSE striking constructional cross-sections was generated (Supporting Information). By applying 3D interpolation and meshing techniques (i.e., the spline curve method), lithological and structural boundaries were interpolated between the constructional cross-sections and continuous 3D spatial information derived from: (i) lithostratigraphic and structural contacts of model units exposed between ~400 and ~4200 m a.s.l.; (ii) borehole and railway tunnel logs from the Lötschberg–Gotthard transect; and (iii) all available seismic data. Following this approach, the 3D tectonic architecture of the Aar Massif was modelled with an explicit approach incorporating all available field observations, structural analyses at the outcrop scale, tunnel and literature data, as well as large-scale seismic

profiles from the NFP20 atlas and 3D tomographic imaging (*Pfiffner et al.*, 1997; *Diehl et al.*, 2021).

3.3 Cross-section Restoration and 4D Reconstruction

To reconstruct the tectonic evolution of the Aar Massif during the Alpine collision (22 – 0 Ma), six NNW-SSE cross-sections, extracted from the 3D model (see traces AA' to FF' in Figure 1), were retro-deformed by line-balancing (i.e., for the crystalline basement – sedimentary cover contact; Supporting Information). Furthermore, peak temperature data, compiled by *Nibourel et al.* (2021a) estimated by crystallinity of carbonaceous matter, lying within 4 km of the sides of each section and close to the cover-basement contact, were selected and normally projected onto the sections (the data points used for each cross section are available in the Supporting Information). The peak temperature data were restored along with the cross-sections to obtain a paleogradient of the basement units at 22 Ma.

The cross-section restoration involved five assumptions: (i) constant length of top-basement and constant area of the crustal basement in cross-section view; (ii) the pre-collisional geometry of the proximal part of the European passive continental margin was bent by ~10° below the tectonically active boundary of the overriding Helvetic nappes, based on the study of *Nibourel et al.* (2018, 2021b). These studies indicate that the intersection angle between inferred isograds and the top basement, as well as the basal Helvetic thrust, ranged from 10° to 15°, implying that both marker horizons at peak temperature dipped southward at this angle; (iii) no significant Alpine deformation affected the basement units of the Aar Massif prior to the thermal peak. This assumption is supported by the data and thermo-kinematic models of *Nibourel et al.* (2018, 2021a), which build upon and integrate the earlier findings of (*Burkhard*, 1988), *Rahn and Grasemann* (1999), and *Glotzbach et al.* (2010); (iv) constant mean topographic elevation throughout the restored sections, as stated by *Campani et al.* (2012) and *Schlunegger and Kissling* (2015); (v) the location of Permo-Carboniferous and sedimentary wedges (Figures 1, 3, and 4) served as markers for the locations of syn-rift faults. This assumption is supported by field observations of Jurassic extensional structures in multiple Permo-Carboniferous and sedimentary wedges across the massif (e.g., Susten, Windgälle, Tödi, and Gastern, see e.g., *Rohr*, 1926; *Nibourel et al.*, 2021b). The throws of the normal faults were reconstructed using as a minimum estimate the vertical extent of the multiple sedimentary wedges and Permo-Carboniferous troughs (for details see *Musso Piantelli et al.*, 2022).

The retro-deformation was performed considering five time-stages: 0 (present), 10, 15, 18, and 22 Ma. During the 0 to 10 Ma time-interval, a transpressional regime defined by strike-slip to oblique movements was active in the southwestern units of the massif (*Wehrens et al.*, 2016, 2017). The displacement is difficult to quantify in the field as it is partitioned into a large number of shear zones. However, at the contact between the sedimentary cover and the basement in the western Aar Massif, the displacement is limited to a few meters (Figure 1; note that the major Rhone-Simplon related strike-slip displacements occurred in the Rhone valley, therefore, its impact on the Aar Massif basement units was limited; see 3D model of *Campani et al.*, 2014). For this reason, the strike-slip phase was neglected for Aar Massif internal deformation and corresponding out-of-plane movements were not included in the overall estimation of shortening and exhumation of the basement units. We note also that local back-thrusting occurred along parts of the southern boundary of the Aar Massif (see D4 in *Nibourel et al.*, 2021a). This deformation is responsible for the north-westward dip of the southern boundary in some areas (see section BB' and sections $\gamma\gamma'$, and $\delta\delta'$ in the Supporting Information). Because this local back-thrusting involved only minor displacements, these deformation structures were not included in our retrodeformation model.

Each cross-section resulting from the retrodeformation at the above-mentioned time stages was then integrated in Move™. 3D interpolation was subsequently applied between the reconstructed sections to produce a 3D model of each stage of retrodeformation, which were finally combined into a 4D model.

4 Results

In this section, a new structural map of the exposed basement units and a DEM of the top of the basement units derived from the 3D geological model constructed for this study (Figures 4 and 6) reveal the present-day half dome-shaped architecture of the Aar Massif. A simplified downsampled, 3D representation of the Aar Massif model built for this study can be visualised here: https://skfb.ly/pA8Qx or from the swisstopo 3D viewer: https://viewer.swissgeol.ch/ (see also Supporting Information). The results of the cross-section restorations are presented as a 4D, stepwise evolutionary sequence, assuming an in-sequence, south-to-north propagation of deformation affecting the basement units of the massif from 22 Ma to the present (Figure 7). As already outlined in the geological setting section this assumption is supported by the following observations and arguments: (i) *Nibourel et al.* (2021a, and references therein) documented that early thrust faults currently exposed at the highest elevations formed during the early stages of exhumation of the massif are overprinted and rotated by subsequent steep to subvertical reverse faults formed in the central regions of the massif (D3; *Nibourel et al.*, 2021a). (ii) *Mock* (2014); *Wehrens et al.* (2017); *Herwegh et al.* (2020); *Musso Piantelli et al.* (2023) showed that the late thrust faults currently exposed at northernmost regions of the massif cut and post-date the northernmost exposed reverse faults, recording a younger phase of deformation (e.g., Figure 5e). (iii) The lowest thrusts, imaged in seismic profiles (NFP20; *Pfiffner et al.*, 1997) and 3D tomographic models *Diehl et al.* (2021), cut and offset an already steepened and partially

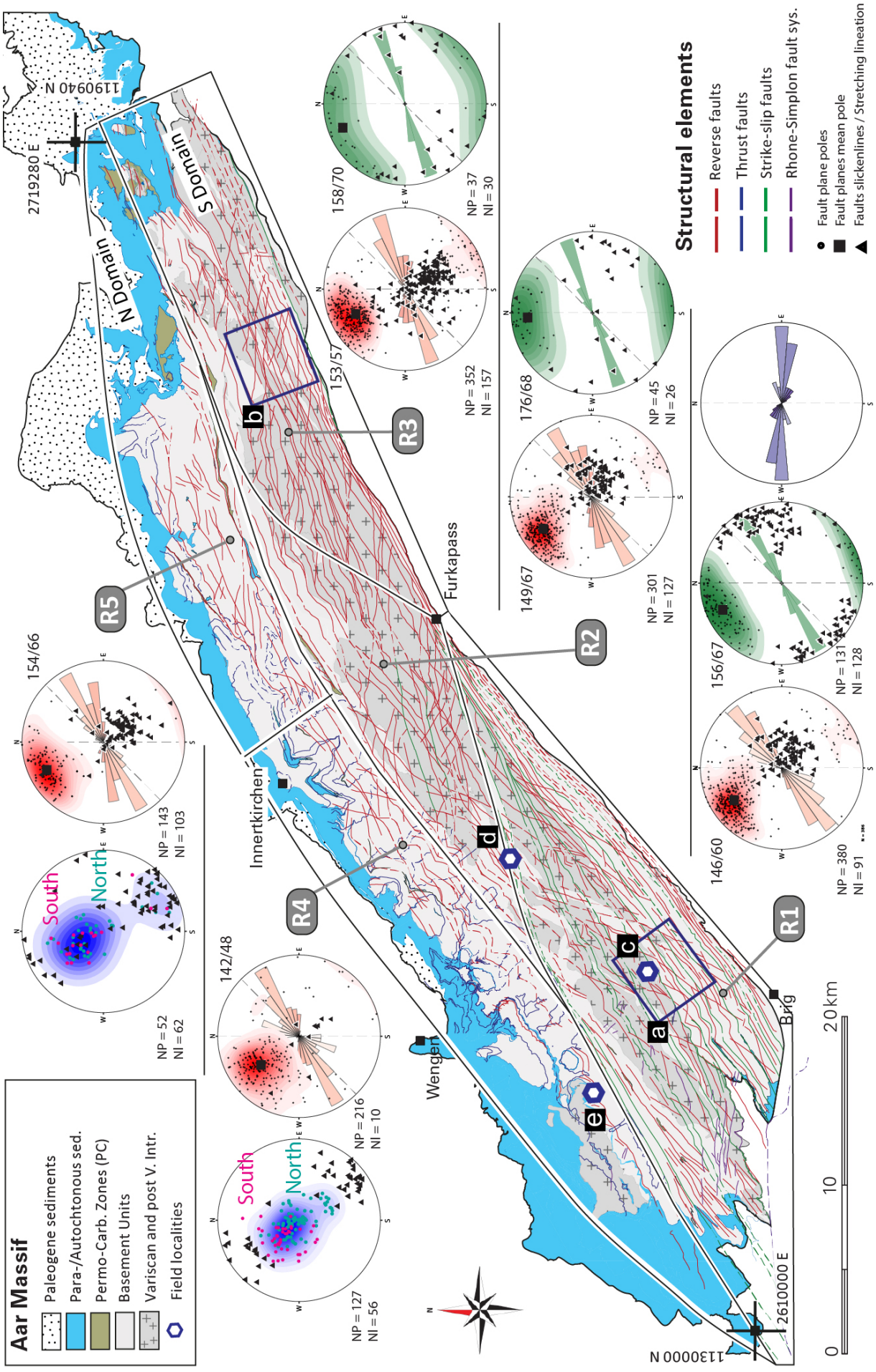
Aar Massif
Paleogene sediments
Para-/Autochtonous sed.
Permo-Carb. Zones (PC)
Basement Units
Variscan and post V. Intr.
Field localities
Structural elements
Reverse faults
Thrust faults
Strike-slip faults
Rhone-Simplon fault sys.
Fault plane poles
Fault planes mean pole
Faults slickenlines / Stretching lineation
N Domain
S Domain
Furkapass
Innertkirchen
Wengen
Brig
R1
R2
R3
R4
R5
a
b
c
d
e
2719280 E
1190940 N
2610000 E
1130000 N
0
10
20km
154/66
NP = 143
NI = 103
South
North
NP = 52
NI = 62
142/48
NP = 216
NI = 10
South
North
NP = 127
NI = 56
158/70
153/57
NP = 37
NI = 30
NP = 352
NI = 157
176/68
149/67
NP = 45
NI = 26
NP = 301
NI = 127
156/67
146/60
NP = 131
NI = 128
NP = 380
NI = 91

Figure 4 – Structural map of the Aar Massif, showing the main fault pattern and the field localities of Figure 5. As outlined in Section 2, the term 'faults' refers to both brittle faults and ductile shear zones. The faults are classified according to their kinematics into: reverse faults (red), thrust faults (blue), dextral strike-slip faults (green) and Rhone-Simplon fault system (purple). The massif is subdivided into five structurally consistent domains R1 to R5. On the sides of the map, the stereoplots show the fault planes poles, mean poles and slickenlines /stretching lineations for each domain. In R4 and 5, note that in the stereoplots of the thrust faults, as highlighted by the color code of the poles, the fault planes progressively increase their dip angle from north to south

exhumed northern front of the massif and correlate with young thrusting in the Subalpine Molasse (8-5 Ma).

4.1 Structural Map of the Aar Massif

The more than 120 km long axis of the Aar Massif shows a bent in the central regions, along a NW-SE trending line between Innertkirchen and Furkapass (Figure 4). The shear zone map presented in Figure 4 shows the distribution of Alpine deformation structures arranged in networks of faults. Most of the structures described are limited in width (dm to few m) but are very persistent in length and often traceable over several kilometres (Figure 5, see also *Steck*, 1968; *Choukroune and Gapais*, 1983; *Wehrens et al.*, 2016, 2017; *Herwegh et al.*, 2017, 2020; *Nibourel et al.*, 2021a). According to the orientations and kinematics characterised in the field, we subdivide the Aar Massif into five structural regions (named R1-R5; Figure 4). Regions R1, R2, and R3, which belong to the inner domain of the Aar Massif, are dominated by reverse faults (red) and dextral strike-slip faults (green). In contrast, regions R4 and R5, situated in the outer domain (Figure 4) are characterized by thrust faults (blue in Figure 4) and reverse faults.

The fault density generally increases toward the southern boundary of the massif (Figure 5c; *Musso Piantelli et al.*, 2023). Most of the faults are steep reverse faults (red in Figures 4 and 5c), locally reactivated in strike-slip to oblique slip mode, especially in region R1 (green in Figures 4 and 5d). The reverse faults of R1 and R3 show mirror symmetry with respect to the massif's centre (Figure 4). In these regions, two main fault systems bound un- or weakly-deformed rhomboid-shaped basement blocks (Figure 5a, b). In R1 the two systems strike SW-NE and SSW-NNE, while in R3 WSW-ENE and E-W (stereoplots in Figure 4). The central region R2 represents a transition zone between R1 and R3 and is characterised by the coexistence of both reverse fault patterns. Therefore, since the fault systems isolate rhomboid basement blocks, the pattern of reverse faults in the southern domain of the massif has an overall arcuate geometry. This observation is also supported by the rotation of the average dip direction/dip of the reverse fault planes in the three regions from 146/60 (R1) to 153/57 (R3, Figure 4).

Irrespective of the faults' strike and the domain in which they occur, the reverse faults are steeply SE-dipping, with down-dip stretching lineations/slickenlines and kinematic indicators mostly indicating an upward movement of the S-block (stereoplots in Figure 4). Strike-slip reactivation localised mainly along the preexisting SW-NE striking reverse faults (Figure 5d). In R1, where most of the reactivation occurred, stretching lineations/slickenlines and kinematic indicators indicate dextral strike-slip movement. In R2 and R3, however, reactivation is restricted to the southern boundary of the massif (Figure 4) with dextral oblique movements (*Nibourel et al.*, 2021a).

In contrast to the south, the faults of the northern regions R4 and R5 show consistent strike and dip along the strike of the massif (Figure 4). Both regions are dominated by NW-vergent thrusts (formed at angles $<35°$) and reverse faults (Figure 5e). These two sets of faults record a long-lasting evolution and show complex cross-cutting relationships as described in sections 2.2 and 4. Exposed thrust planes in the southern areas of the regions (R4-R5) exhibit a gentle curvature, dipping moderately SW before progressively flattening in the central areas and even gently tilting to the NW towards the northern rim of the massif (e.g., the thrust plane at Jungfrau, Figure 3a; see also Figure 4). In the northern areas of R4 and R5, reverse faults strike SW-NE and dip towards the SE at lower angles than in the southern regions of the massif. These faults are subsequently cut by the thrust faults now exposed at the northernmost regions of the massif Figure 6b; e.g., Figure 5e).

4.2 Overall 3D Shape of the Aar Massif

In this work, a regional 3D geological model of the basement units and main structures of the Aar Massif was built with explicit modelling techniques (for a simplified downsampled 3D visualization click here: https://skfb.ly/pA8Qx or from the swisstopo 3D viewer: https://viewer.swissgeol.ch/; see also Supporting Information). The reconstructed top of the basement shows the half dome-shape of the Aar Massif (Figure 6). Neglecting erosion, the centre of the massif would have reached a maximum elevation of > 6 km a.s.l. However, ~3800 km^3 of basement have been eroded to reach the present day maximum topographic elevation of 4.2 km a.s.l. Permo-Carboniferous, Triassic, Early and Middle Jurassic sediments are aligned along major structures and locally pinched between the basement (Figures 1 and 3c). The erosion of the basement units, coupled with lateral geometric variation has resulted in different degrees of preservation and exposure of these sediment wedges (Figures 1 and 3).

At the northern front, the top basement is dissected by multiple NW-vergent thrust faults and dips steeply to the NW toward the frontal thrust of the massif, which separates it from the largely undeformed basement units underlying the North-Alpine foreland. To the

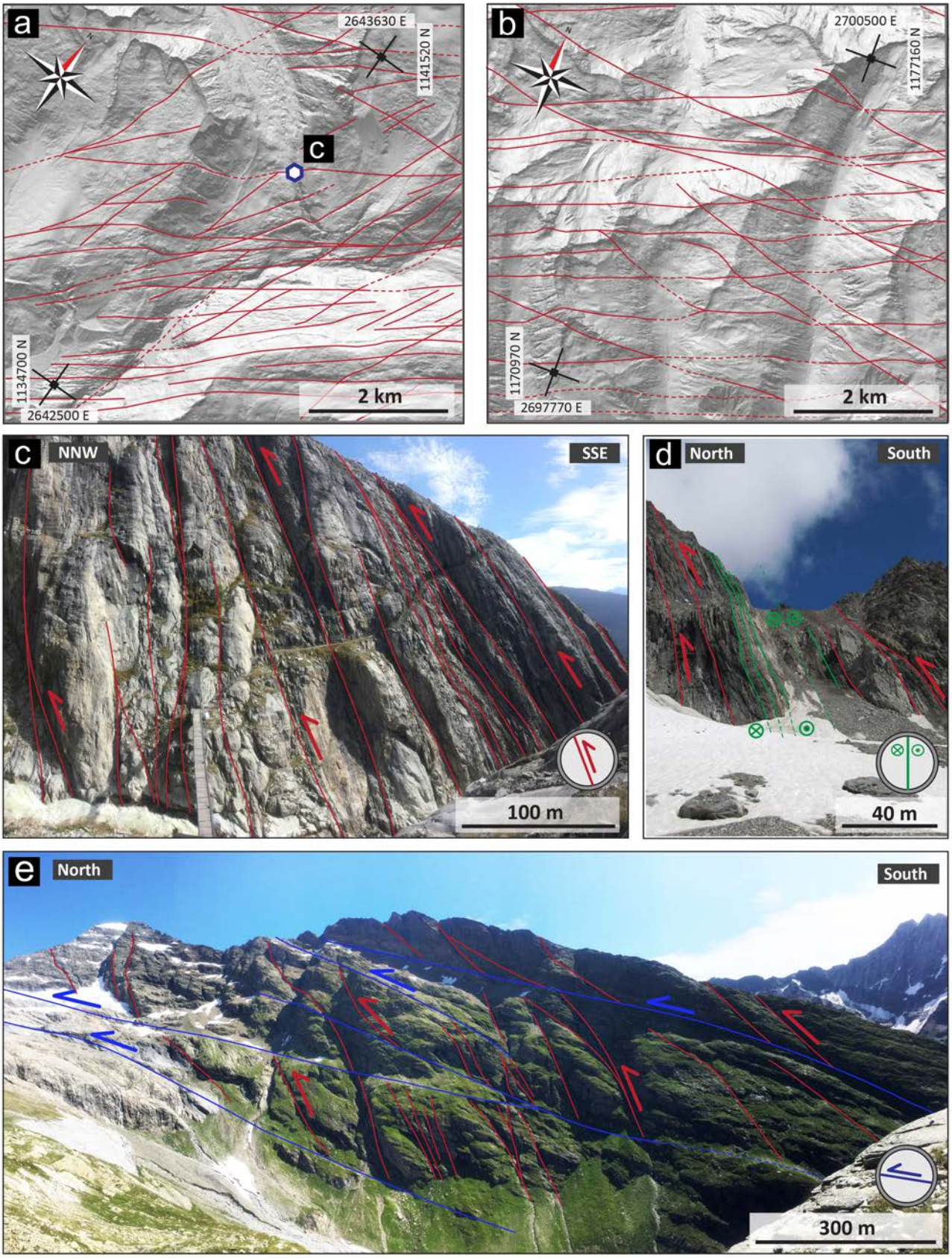

Figure 5 – Sequence of field images of the main characteristic structures of the Aar Massif. Field locations indicated in Figure 4 and coordinates are provided in Supporting Information. (A and B) Details of regions R1 **(A)** and R3 **(B)** with the detected structures on hillshade maps. The two main systems of reverse faults bound large-scale rhomboid blocks, mirrored in regions R1 and R2. **(C)** Gneiss unit dissected by a series of steep reverse fault zones. **(D)** Basement units dissected by steep reverse faults and locally reactivated by dextral strike-slip faults (modified after *Musso Piantelli et al.*, 2023). **(E)** Gneiss unit dissected by thrust faults that cut the reverse faults.

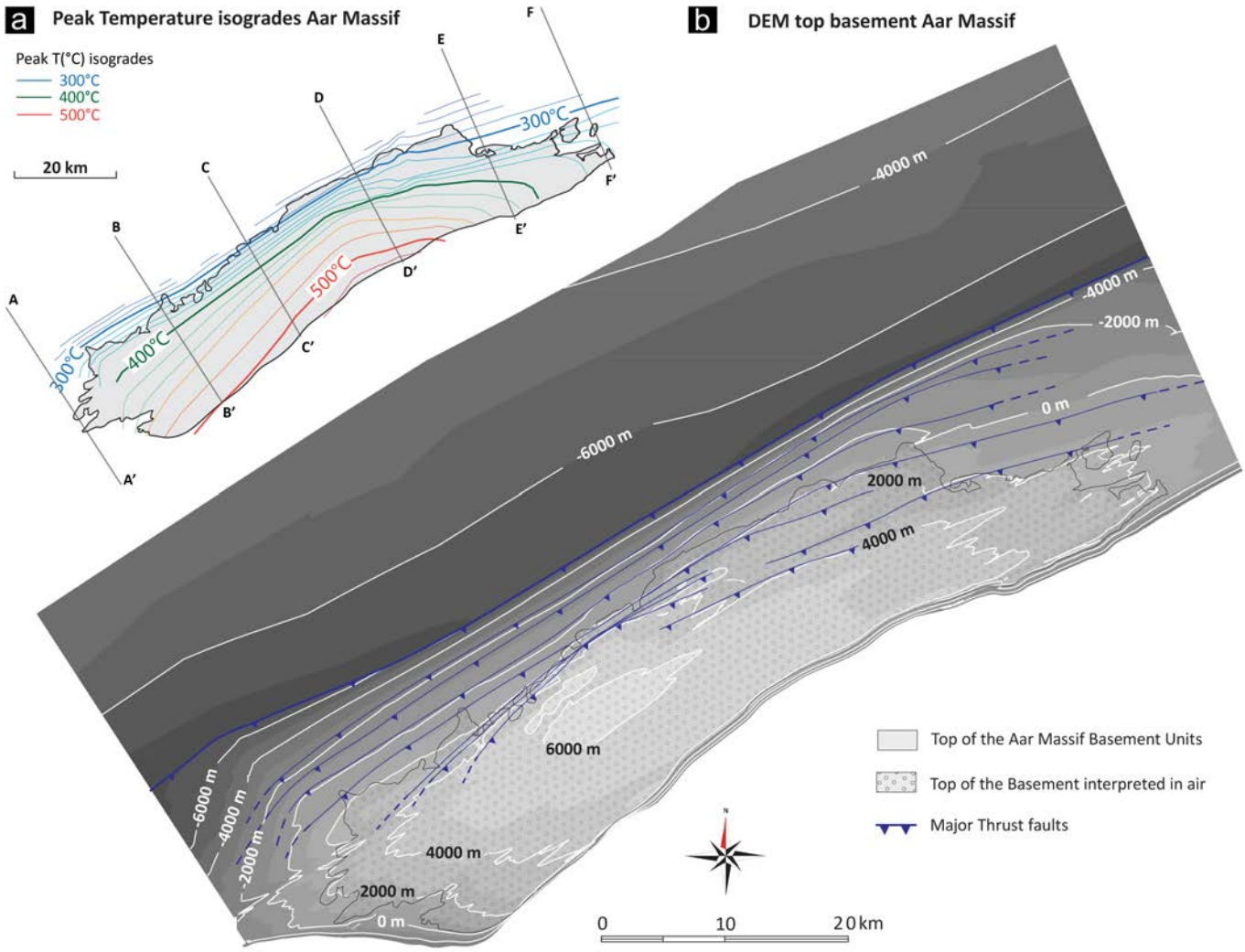

Figure 6 – Map view of the modelled (A) paleo-isotemperature map and (B) top of the crystalline basement units of the Aar Massif. **(A)** Paleo-isotemperature map (published by *Nibourel et al.*, 2021b) showing the peak Alpine metamorphic conditions reached in the massif prior to 22 Ma. The general pattern of isograde at the 1500 m (a.s.l.) elevation level closely follows the trend of the structures (Figure 4) and reflects the three-dimensional architecture of the Aar Massif. **(B)** 2D top view of the half dome-shape of the massif with the central regions exhumed to 6 km a.s.l. and the flanks at –4 km a.s.l. Multiple large-scale thrust faults (blue lines) dissect and steepen the northern front of the massif.

west and east, the massif's top basement gradually plunges to a modelled elevation of -4 km on both sides (Figure 6). This results in an elevation difference of 10 km between the sides and the central region of the massif. The pattern of the paleo peak temperature isograds published by *Nibourel et al.* (2021a) closely resembles the trend of the structures and reflects the three-dimensional half dome-shape of the Aar Massif, both in massif-perpendicular and along-strike directions (Figure 6a).

As shown in Figure 2, the basal thrust is a prominent feature of the Aar Massif. The offset of the basement units is currently estimated from reflection seismic profiles and 3D tomographic imaging (*Pfiffner et al.*, 1997; *Diehl et al.*, 2021). It increases along the strike of the massif from west to east. Indeed, in profile AA' the thrust offsets the basement for ca. 3 km, whereas in profile FF' for ca. 9 km.

4.3 Dynamics of Alpine Deformation

Six NNW-SSE striking geological cross-sections (AA' to FF'; traces in Figure 1) were retro-deformed independently to reconstruct how the Aar Massif reached its present-day geometry. For each retrodeformation stage a 3D model was generated by interpolating the six sections, resulting in a 4D reconstruction of the evolution of the Aar Massif in space and time. This section shows the result of the retro-deformation of cross-section D-D', as a representative example (Figure 7, Cross-section view), and the corresponding generated 3D model of the retrodeformation stages (Figure 7, 3D view). The other retro-deformed sections are stored in Supporting Information. Figure 7 is a simplified version of a larger figure (Figure 7 extended) that includes a map view of the evolution in addition to the cross-section and 3D views, which is available here: https://doi.org/10.6084/m9.figshare.31055788.

22 Ma (Figure 7a): At the onset of Alpine deformation the former passive continental margin of the European

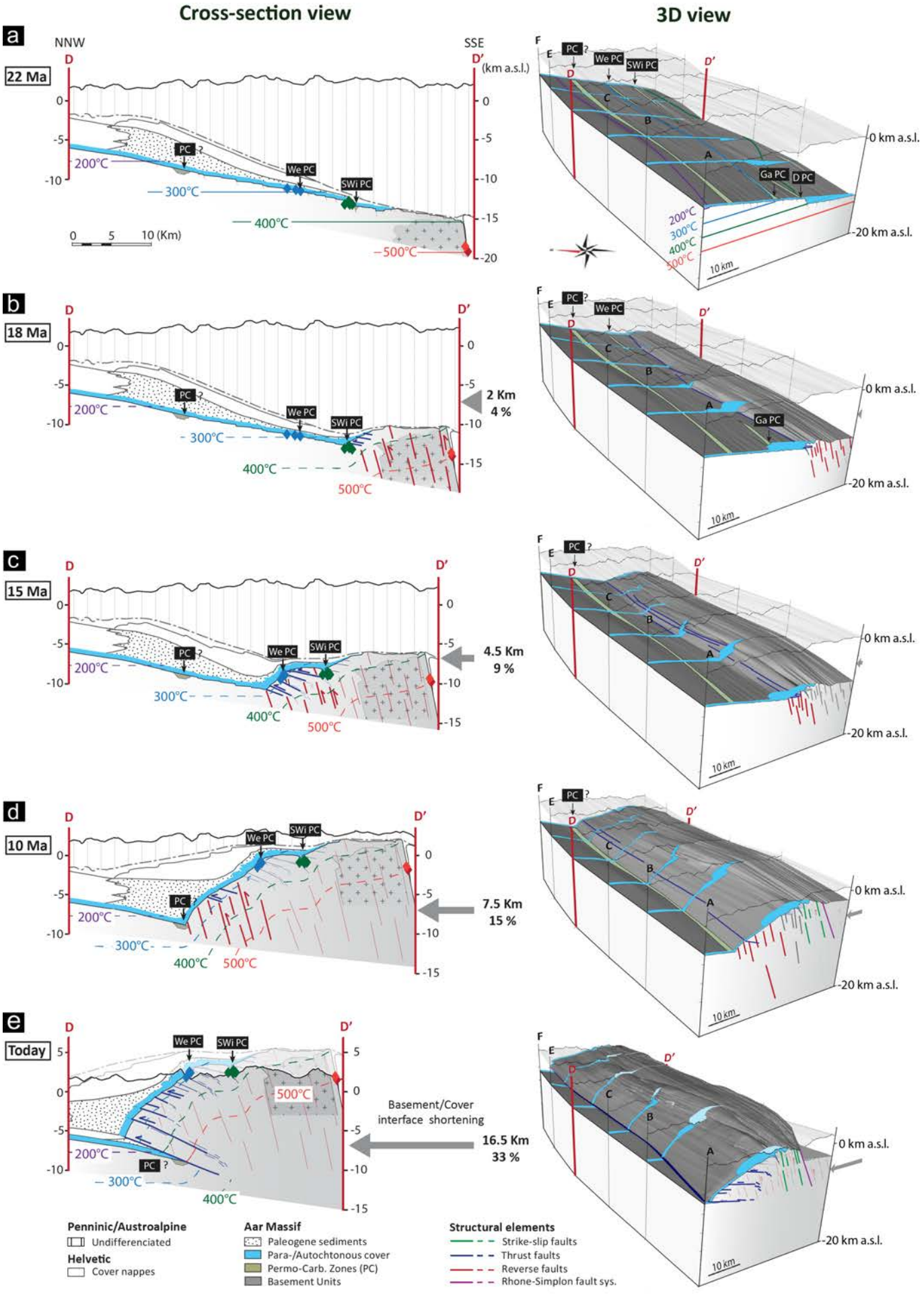
Cross-section view
3D view
a
22 Ma
NNW
SSE
D
D'
(km a.s.l.)
PC ?
We PC
SWi PC
200°C
300°C
400°C
500°C
0 5 10 (Km)
Ga PC
D PC
0 km a.s.l.
-20 km a.s.l.
10 km
b
18 Ma
2 Km
4 %
c
15 Ma
4.5 Km
9 %
d
10 Ma
7.5 Km
15 %
e
Today
Basement/Cover
interface shortening
16.5 Km
33 %
Penninic/Austroalpine
Undifferenciated
Helvetic
Cover nappes
Aar Massif
Paleogene sediments
Para-/Autochtonous cover
Permo-Carb. Zones (PC)
Basement Units
Structural elements
Strike-slip faults
Thrust faults
Reverse faults
Rhone-Simplon fault sys.

Figure 7 – 3D geological model and cross-section restoration of the D-D' section from 22 Ma to the present. For each deformation stage, the corresponding active deformation phase is indicated by thicker line and distinct colour. Reverse faults are shown with a patterned style due to their high frequency and dense distribution. **(A)** At 22 Ma, the massif is situated beneath the Helvetic, Penninic and Austroalpine nappes, as well as Paleogene sediments to the north. **(B)** At 18 Ma, the southern region of the massif was exhumed by the formation of steep reverse faults (red lines) and thrust faults (blue lines). **(C)** At 15 Ma, the exhumation of the basement units proceeded to the central region of the massif, with the formation of subvertical reverse faults and shallow-dipping thrusts. **(D)** At 10 Ma, the exhumation advanced to the northern region of the massif, with a strong reverse fault component. This phase resulted in the formation of the steep northern front of the massif and the passive up-doming of the overlying nappe stack. **(E)** From 10 Ma onwards, flat- to moderately SE-dipping thrust faults (blue lines) dissected the basement units. This resulted in an 'en bloc' exhumation (*Herwegh et al.*, 2020, 2024; *Nibourel et al.*, 2018, 2021b) of the basement units with ~9 km of shortening. A larger version of this figure including a map view is available here: https://doi.org/10.6084/m9.figshare.31055788.

plate was bent by ~10° and buried at a maximum depth of -15 km in the footwall of the overriding nappes (*Ebert et al.*, 2008; *Nibourel et al.*, 2018, 2021a). In the lower plate, the interpolation of the retrodeformed peak temperature data (compiled by *Nibourel et al.*, 2021a) resulted in near-horizontal isotherms with an average geothermal gradient of 26°C/km (Supporting Information). Along the strike, the basement units were dissected by normal faults, still visible in the field (as described with field data by *Nibourel et al.*, 2021a), often associated with former Permo-Carboniferous half grabens (e.g., *Burkhard*, 1988; *Musso Piantelli et al.*, 2022). To the sides of the massif, sections AA', BB' and EE', FF', the large volume of Autochthonous and Parautochthonous sediments was deposited into large basins. In the central regions, sections C-C' and D-D' reveal a topographic high with absence of large basins and small volumes of sediments.

22 - 18 Ma (Figure 7b): Uplift of the basement units began at 22 Ma in the southern regions of the developing massif with the formation of steep reverse faults (red lines) and thrust faults (blue lines). The reverse faults developed in the basement units forming rhomboid basement blocks. Such faults, as described in field data by *Nibourel et al.* (2021a), did not, or only weakly reactivate the south-dipping Jurassic extensional normal faults. Along the strike, the reverse faults had larger displacement in the centre compared to the sides of the massif (see also section 4.4). The central regions of the massif were uplifted to a depth of -10 km, while the sides remained buried at about -12 km, developing an early stage of the half dome-shape of the massif (see Figure 7 extended: https://doi.org/10.6084/m9.figshare.31055788). The thrust faults were localised at the front of this southern region, directed by the presence of the major Susten-Windgälle and Doldenhorn Permo-Carboniferous troughs (Figures 1, 2 and 7). Together, the reverse and thrust faults produced what today corresponds to the highest exposed thrusts in the Aar massif, as for example the Windgällen complex and the Susten and Jungfraukeil synformal wedges of Mesozoic and Permo-Carboniferous sediments, with steeply dipping and locally overturned strata (e.g., Figure 3a, c; see also D4, D3 *Nibourel et al.*, 2021a).

18 - 15 Ma (Figure 7c): With ongoing convergence, exhumation of the basement units progressed towards the central regions of the massif. Steep to sub-vertical reverse faults and shallow-dipping thrusts were active thus exhuming top basement to a depth of about -6 km in the centre and -10 at the E- and W-sides of the massif. The reverse faults overprint and locally rotate the thrust faults developed during the previous time interval (D4, D3 *Nibourel et al.*, 2021a, and reference therein). Thrust faults localised at the front of the central region where the Wenden and Gastern Permo-Carboniferous troughs were located. Such thrust faults cut and dislocate the reverse faults developed at the front of the exhumed massif (D3 *Nibourel et al.*, 2021a,b). As a result, such reverse faulting and thrusting produced what today corresponds to the intermediate level of exposed thrusts in the Aar Massif, such as, Wetterhorn and Gastern (Figures 1, 2 and 7) synformal wedges of Mesozoic and Permo-Carboniferous sediments.

15 - 10 Ma (Figure 7d): Basement exhumation moved into the northern units of the massif. Beginning around 13-12 Ma, thrusts that are now exposed in the northernmost regions of the massif developed, cutting and displacing the reverse faults formed during the previous stage. For additional information, see the Pfaffenchopf faults described by *Mock* (2014), *Wehrens et al.* (2017), *Herwegh et al.* (2020), *Nibourel et al.* (2021a,b), and *Musso Piantelli et al.* (2023). The accumulated reverse faulting and thrusting over this and the previous stages caused the steep north-dipping top basement at the northern front of the massif and the passive up-doming of the overlying Helvetic/Penninic nappe stack. Most of the structures which formed during and after this interval remain buried at depth are not exposed at the surface today (see Figure 2). For this reason, no field information can be provided, and the thrusts and reverse faults are inferred from large-scale seismic profiles (NFP20; *Pfiffner et al.*, 1997) and 3D tomographic imaging (*Diehl et al.*, 2021). In the central northern Aar Massif, top basement descends from an elevation of 2 km to an elevation of -8 km over a horizontal distance of a few kilometers. At the W- and E-sides the top basement dips toward the N more gently from 0-2 km to -8 km. In the south western regions of the massif, reactivation of the reverse faults in dextral strike-slip mode initiated (green lines Figure 7d, e). During the same period, transtensional movements along the Rhone Simplon fault system were documented (Purple line in Figure 7d,e; *Grosjean et al.*, 2004; *Campani et al.*, 2014; *Cardello et al.*, 2024).

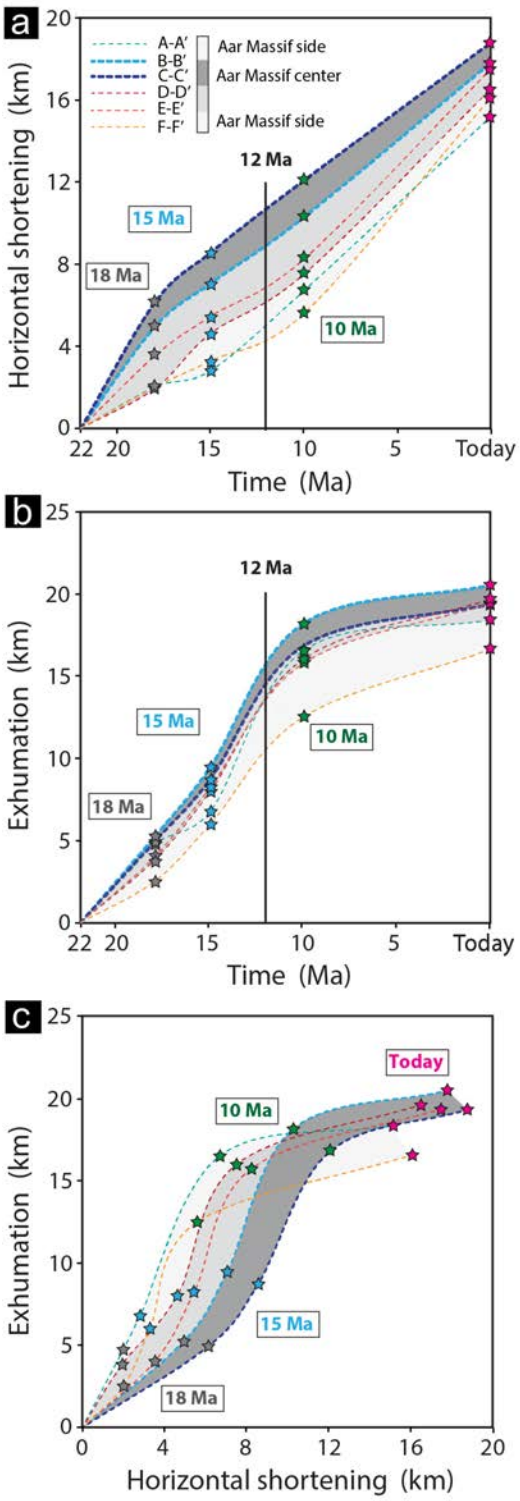

Figure 8 – Plots of horizontal shortening **(A)** and exhumation **(B)** calculated from the trajectories of the highest-elevation points of the present-day basement–cover interface (dashed lines) along six cross sections throughout the restoration time intervals. **(A)** Horizontal shortening was greater in the central units than in the flanks of the massif. **(B)** The plot of the exhumation of the basement units shows a strong exhumation component between 22 and 12 Ma, followed by a decrease after 12 Ma. **(C)** The plot of the combination of horizontal shortening and exhumation shows that the central units of the massif (dark grey area) generally experienced greater exhumation and shortening than the flanks (light grey).

10 Ma - today (Figure 7e): In contrast to previous time intervals, reverse faulting is no longer active after 10 Ma (*Herwegh et al.*, 2020, 2024). In the north of the massif, horizontal to moderately SE-dipping thrust faults (blue lines) dissected the northern front and accommodated NW-SE-directed shortening. The deformation was mostly localised at the base of the massif, forming a large-scale thrust that uplifted the massif up to 6 km in the centre and ~2 km on the sides. These deeper thrust faults are not exposed today (see Figure 2) and are inferred from large-scale seismic profiles (NFP20; Pfiffner et al., 1997) and 3D tomographic imaging (*Diehl et al.*, 2021). At the same time, strike-slip reactivation of the reverse faults was also active in the SW (green lines Figure 7d, e), as was the Rhone Simplon transtensional system, which dissected the south-western edge of the massif by ~2.5 km of vertical offset (Purple line in Figure 7d,e; *Grosjean et al.*, 2004; *Campani et al.*, 2014; *Cardello et al.*, 2024).

4.4 Horizontal Shortening and Vertical Uplift

The plots in Figure 8 show the horizontal shortening and vertical uplift components recorded by the trajectories of the present-day highest point in elevation of the basement-cover interface in the six retro-deformed sections over the relative time intervals. Horizontal shortening and vertical rock uplift of the Aar Massif were both initiated at 22 Ma with the onset of reverse faulting and thrusting. The deformation recorded by the basement-cover interface is characterised by a shortening component of 15 to 19 km and an uplift component of 16.5 to 20.5 km (Figure 8a and b). These values correspond to an average shortening rate of 0.7 mm/yr and uplift rates of 0.9 mm/yr. However, the cumulative trajectory of each section shows that the central units of the massif have experienced greater uplift and shortening than the western and eastern flanks of the massif (dark grey field in Figure 8c).

Shortening rates (Figure 8a) between 22 Ma and 12-10 Ma range from 0.46 to 0.98 mm/yr, and show a stronger shortening component in the centre than in the west and east. From 12-10 Ma to the present, the shortening rates increase to 0.67 - 1 mm/yr with now higher shortening rates at the E- and W-sides of the massif than central region.

Uplift rates (Figure 8b) between 22 Ma and 12-10 Ma range from 1.1 to 1.5 mm/yr and are higher in the centre, decreasing towards the eastern and western flanks of the massif. From 12-10 Ma to the present, uplift rates decrease drastically and progressively from east (0.4 mm/yr) to west (0.18 mm/yr) along strike.

5 Discussion

The results obtained by restoring the six cross-sections and the corresponding 3D model generated for each stage of retrodeformation provide new insights into the 4D geodynamic evolution of the Aar Massif and into the broader perspective of the External Crystalline massifs

of the European Alps from a passive continental margin to their emplacement within the orogen.

5.1 The Aar Massif, as a Portion of the European Passive Margin

The Aar Massif was located on the proximal European passive continental margin. As observable in present-day examples of the mid-Norwegian, Iberian, or Angola-Gabon proximal domains along the Atlantic rift system, such regions of extensional tectonics are characterised by weakly developed rift-related lithospheric and crustal thinning (e.g., *Mohn et al.*, 2011; *Peron-Pinvidic et al.*, 2013). The generation of accommodation space is, therefore, restricted to graben and half-graben basins (e.g., *Wilson et al.*, 2001; *Tugend et al.*, 2015). This tectonic scenario fits well with our reconstructed 3D architecture of the Aar Massif segment of the European passive continental margin (Figure 9). As described in section 3.3, the locations and vertical extent of the multiple sedimentary wedges and Permo-Carboniferous troughs (Figures 1, 3, and 4) served as markers for the locations of syn-rift faults and the formation of Mesozoic half-graben basins. The latter were named after the deriving nappes or geographic location.

The reconstructed passive margin represented in Figure 9 exhibits a prominent topographic high highlighted by the black contour line and, at the sides, three asymmetric half-grabens called the Doldenhorn, Susten-Windgällen, and Tödi-half grabens. The basement high is referred to as 'Aar topographic high', coinciding with a southern promontory of the Alemannic Land (see Figure 9b and c; *Trümpy*, 1952). The basins were bounded by northeast-southwest trending, southeast-dipping normal faults (e.g., Figure 3c). Such normal faults are still preserved in the field at some locations in the Aar Massif and have been described by several authors (e.g., *Rohr*, 1926; *Nibourel et al.*, 2021a). As indicated by thickness variations in the sedimentary wedges distributed within today's Aar Massif. The estimated throw of these normal faults was larger at the W- and E-sides of the massif (up to about 2 km) and decreased towards the Aar topographic high in the centre (a few hundred metres; Figure 9b, c; *Musso Piantelli et al.*, 2022).

This asymmetric rifting scenario resulted in differential tectonic subsidence, which had a direct impact on the volumetric disposition and stratigraphic thickness of the para- and autochthonous sedimentary units of the massif. Up to 2 km thick sedimentary sequences were deposited in the basins, at the sides of the massif, whereas only a few hundred metres thick sedimentary sequences were deposited onto the Aar Massif topographic high (Figure 9c; see also *Kempf and Adrian Pfiffner*, 2004; *Cardello and Mancktelow*, 2014; *Musso Piantelli et al.*, 2022). This palaeogeographic reconstruction explains the thickness variation of the Aar Massif's para- and autochthonous sedimentary cover in the orogen-parallel direction (Figure 2). Furthermore, it indicates that the present-day 10 km elevation difference from sides to centre of the Aar Massif (see paragraph 4.2) was inherited in part (20%) from the passive margin geometry. Indeed, prior to the onset of the Alpine collision, an elevation difference of the basement-cover contact of about 2 km existed between the evolving massif's sides (basins) and the Aar basement high (Figure 9b).

Besides this large-scale 3D margin architecture, the reconstruction highlights a direct link between Mesozoic margin topography/basin asymmetries and the pre-existing crustal structures of the basement units imposed by the multiple Permo-Carboniferous troughs (e.g., *Santantonio and Carminati*, 2011; *Lafosse et al.*, 2016; *Balázs et al.*, 2017). The large number of wedges with Mesozoic sediments associated with the occurrence of the pre-existing Permo-Carboniferous troughs (e.g., Figure 3c) indicates a strong correlation between Mesozoic normal faulting and inherited crustal structures (*Berger et al.*, 2017a). This suggests that the geometry of the European proximal continental margin was largely controlled by the localisation of normal faults within pre-existing Late Carboniferous-Permian crustal structures (see also, e.g., *Badertscher and Burkhard*, 1998; *Masini et al.*, 2013; *Ballèvre et al.*, 2018; *Nibourel et al.*, 2021a; *Musso Piantelli et al.*, 2022). In the case of the Aar Massif, the Susten-Windgälle, Doldenhorn, Wenden, Gastern Permo-Carboniferous troughs and a hypothesised trough at the front of the future massif, divide the margin into three major large-scale crustal blocks (Figure 9b). On the western and eastern sides of the massif, the block boundaries were dissected by major Mesozoic normal fault. In contrast, the central part of the massif experienced only limited fault offset, on the order of a few hundred meters, resulting in less pronounced block boundaries. Notably, despite the Mesozoic extension, overall crustal thinning remained moderate, leaving basement thicknesses of about 25-27 km, which are values close to the normal crustal thickness of undisturbed continental crust. For a classical passive margin geometry (e.g., *Mohn et al.*, 2012), the Aar Massif, like the other External Crystalline Massifs, therefore represented the proximal part of the European passive continental margin (see also *Herwegh et al.*, 2024). Substantial crustal thinning occurred farther south, corresponding to the distal margin domains now represented by the Gotthard nappe and the Lepontine gneiss nappes (e.g., *Steck*, 2008).

The reconstructed local geometry of the Mesozoic Aar Massif paleogeography may also have implications for the plate tectonics scale of the proximal European Passive continental margin and its associated rift kinematics: (1) Belledonne, Aiguilles Rouges/Mont Blanc and Aar Massifs are all lentoid in shape with their axes parallel to the former plate margin (Figure 9a; e.g., *Herwegh et al.*, 2024). (2) The Aar Massif grades laterally into basins at the western and eastern side, whereby both depth and width diminish gradually towards the Aar basement high. (Figure 9b,c). (3) In a similar way all the other massifs form a laterally discontinuous belt of basement domes which are separated by structural saddles, see for

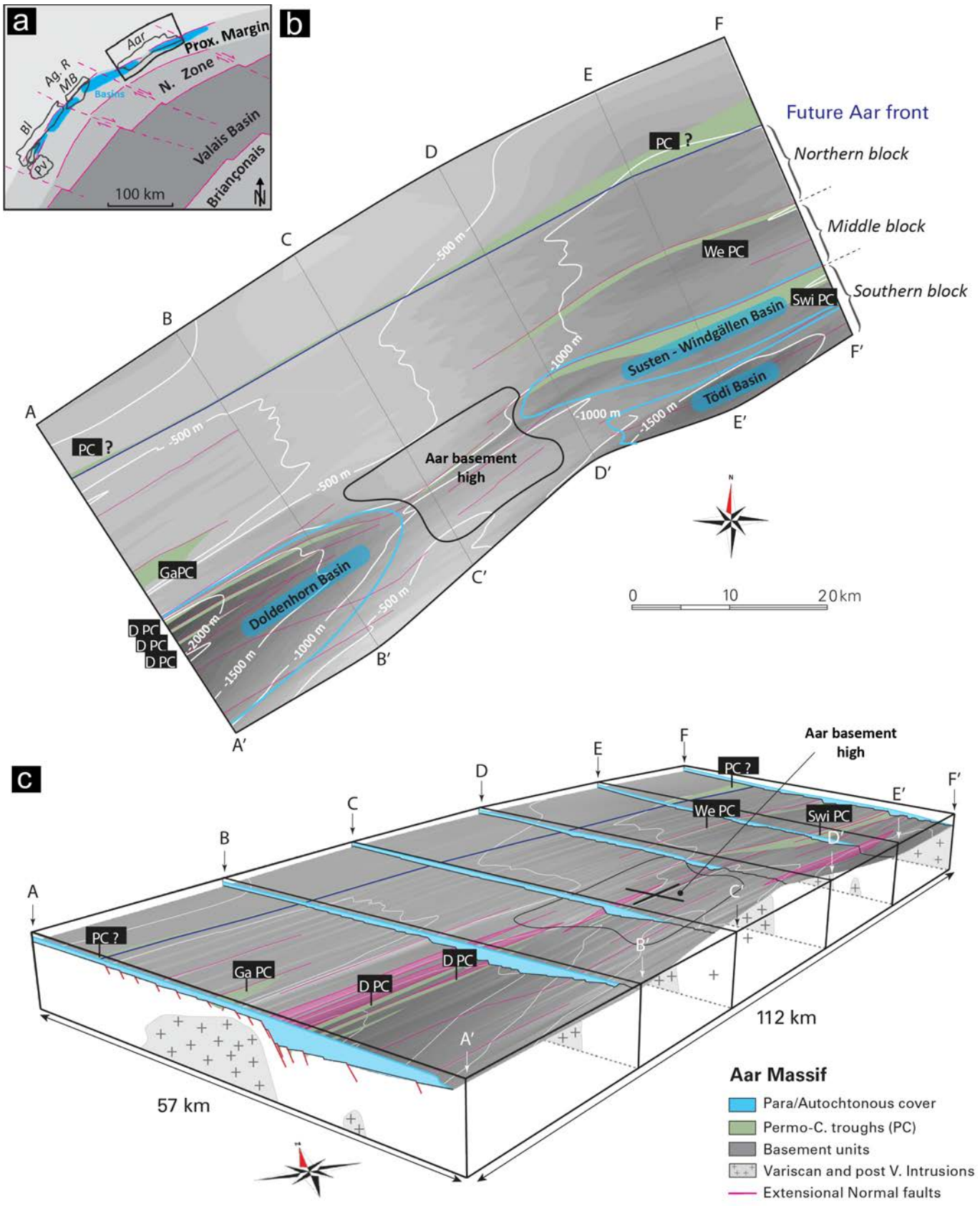

Figure 9 – Map and 3D block reconstruction of the restored passive margin. **(A)** inset modified after *Handy et al.* (2010). **(B)** Map view of the top basement units of the reconstructed passive margin. The elevation contour highlights the ~2 km elevation difference between the Aar basement high and the basins on both flanks. The map view shows the subdivision of massif blocks and highlights the strong control of Permo-Carboniferous troughs. **(C)** 3D block reconstruction of the restored passive margin and sediment basins. A series of Jurassic normal faults opened three asymmetric half-grabens on the western and eastern flanks of the margin, respectively. This asymmetric rifting scenario controlled the accommodation space for para-/autochthonous sediment deposition, resulting in thicker units in the basins and a thinner cover over the basement high.

example the top basement isohypse maps of *Pfiffner et al.* (2011).

These features (1–3) have already been recognized by *Burkhard* (1988) and *Pfiffner et al.* (2011), who inferred a dextral transfer fault between the Aar Massif and the Aiguilles Rouges/Mont Blanc massifs. As a possible interpretative model, we suggest that such a geometry may be explained by an initial stage of oblique rifting between Europe and Adria (*Herwegh et al.*, 2024, and references therein), with sequential pull-apart basins developing between basement highs (Figure 9a). This scenario is consistent with patterns observed in oblique rift systems reproduced in analogue modelling experiments (e.g., *McClay and White*, 1995; *Mart and Dauteuil*, 2000; *Corti et al.*, 2007). We emphasize, however, that this should be regarded as a conceptual model since such transfer zones are largely buried beneath thick sedimentary successions and thus cannot be directly observed.

5.2 Peak Temperature and P-T Conditions

The general pattern of the Alpine peak temperature isograds recorded in the study area (*Nibourel et al.*, 2021b) closely resembles the three-dimensional half dome-shape of the massif and the trend of the exhumation-related structures (compare Figures 4 and 6). These observations support the interpretation that most of the Alpine deformation and the associated development of the present structural relief occurred after the peak temperature conditions, which is also generally consistent with the data and thermo-kinematic models of *Nibourel et al.* (2018, 2021a), which build upon and integrate the earlier findings of *Burkhard* (1988), *Rahn and Grasemann* (1999), and *Glotzbach et al.* (2010).

Retrodeformation along the six cross-sections of the peak temperature data allowed reconstruction of the paleo-gradient of peak temperature conditions before the onset of Alpine deformation (22 Ma, Figure 10a). Interpolation of the retrodeformed peak temperature data indicates in this portion of the margin an average geothermal gradient of 26°C/km (Supporting Information). Peak metamorphism in the study area was reached by burial in the footwall to the basal Helvetic thrust, the main active tectonic boundary at the time, above which was situated the ca. 15km thick Alpine nappe stack of Helvetic, Penninic and Austroalpine nappes (Figure 7a; *Pfiffner*, 2024). By assuming near-horizontal isograds during peak metamorphism, the peak-temperature becomes a key constraint, defining the depth of our retrodeformed continental margin prior to the onset of Alpine contractional deformation. Note that in a setting with rapid tectonic movements, heat advection could result in oblique or locally even inverted thermal gradients (e.g., *Girault et al.*, 2020). However, numeric models (e.g., *Shi and Wang*, 1987) indicate that thermal perturbations across low-angle thrusts such as the basal Helvetic thrust, having slip rates lower than 5 mm/a re-equilibrate rapidly, (*Nibourel et al.*, 2021b; *Pfiffner*, 2024). Although minor temperature perturbations cannot be excluded, this supports the assumption of an overall steady geothermal gradient of about 25°/km depth around peak metamorphic conditions. The peak-temperature at maximum burial conditions of the reconstructed sedimentary–basement contact along the margin shows a pronounced north-to-south increase, rising from 240°C in the north to 380–460°C in the south (Figure 7 extended: https://doi.org/10.6084/m9.figshare.31055788). Along the strike of the southern regions, temperatures increased from 380°C in the centre to up to 460°C on the sides of the massif, at a depth ranging between 18-20 km, reflecting the inherited topography of the passive margin (see 400°C isograd line in Figure 10a). Such reconstruction is in good agreement with the thermochronometric and structural data of *Nibourel et al.* (2021b); *Berger et al.* (2020); *Herwegh et al.* (2017, 2020) and the pressure estimate of 6.5 kbar from *Goncalves et al.* (2012).

5.3 The 4D Geodynamic Evolution of the Aar Massif

In our reconstruction, we propose an in-sequence exhumation of the basement units, showing how deformation initiated in the southern crustal block of the massif, then migrating gradually towards the northern front of the present-day massif. In the following section, we present the 4D crustal-scale geodynamic reconstruction of the Aar Massif evolution, subdivided into four stages (Figures 7 and 10). The 3D block sketches, based on our 4D model, highlight the active collisional faults and the resulting shortening/uplift of the top crystalline basement that produced the present-day half dome-shape of the massif from 22 Ma to the present.

22–18 Ma: during this initial phase of deformation, steeply south-dipping to sub-vertical reverse faults localised in the southern block of the massif (Figure 10b). The northern limit of the block was defined by the Permo-Carboniferous to Mesozoic and bounding faults of the Doldenhorn and Susten-Windgällen basins (Figures 9a, 10a). The localization of steep reverse faults was induced by buoyancy forces acting on mid- to upper-crustal rocks that were decoupled from the underlying European lower crust and lithospheric mantle (*Herwegh et al.*, 2017, 2020, 2024; *Kissling and Schlunegger*, 2018). Given the greater degree of exhumation observed in the central region of the block, we hypothesise that the buoyancy forces in question were more pronounced in the centre of the massif, where the crust was thicker and less stretched in comparison to the sides of the massif. The resulting reverse faults were localised as a dense network of anastomosing faults that divided the large crustal block into a series of small-scale rhomboidal blocks (Figure 5a, b). The individual rhomboid blocks recorded differential exhumation leading to a larger uplift component in the central, decreasing toward the E- and W-sides of the massif. In addition to the reverse faults, thrust faults were also localised at the northern limit of the block.

It was during this phase that the thrusts currently located at the highest elevation within the Aar massif (Jungfrau, Windgällen and Wetterhorn) were developed (Figure 3; *Butler et al.*, 2006; *Mair et al.*, 2018; *Nibourel et al.*, 2021a). Consequently, a combination of enhanced horizontal shortening and vertical exhumation rates (Figure 8c) in the central region of the block, induced a +4 km uplift of the basement-cover contact relative to its depth at maximum burial (see Figure 10a).

18–15 Ma (Figure 10b, c): Due to the progressive shortening caused by the advancing orogen, differential vertical uplift by reverse faulting gradually shifted northwards to the middle-block of the Aar Massif. Such reverse faults overprinted and rotated the previously developed thrust faults (see *Nibourel et al.*, 2021a). The Wenden and Gastern Permo-Carboniferous troughs mark the northern boundary of this block. (Figures 9b, 10c). At these locations, thrust structures were generated and, together with reverse faulting, they induced a further exhumation of basement units, which was greater in the central regions (+4 km) compared to the western and eastern sides (+2 km). During this deformation event, the thrust faults cut and dislocate the reverse faults developed at the front of the exhumed block (D3; *Nibourel et al.*, 2021a,b). This process produced the thrust systems that are today exposed at intermediate elevations in the Aar Massif, such as Wetterhorn and Gastern.

15–10 Ma (Figure 10c, d): The exhumation of the basement units progressed into the northern crustal block. The reverse faulting induced vertical rock uplift decreasing toward the northern limit of the block. From 13-12 Ma, thrusts that are now exposed in the northernmost regions of the massif developed, cutting and displacing the reverse faults formed during the previous stage. For additional information, see also the Pfaffenchopf faults (*Mock*, 2014; *Wehrens et al.*, 2017; *Herwegh et al.*, 2020; *Nibourel et al.*, 2021a,b; *Musso Piantelli et al.*, 2023). As observed for the southern and middle blocks, we hypothesise that the limit of the northern block of the massif was marked by the presence of a Permo-Carboniferous trough. However, this hypothesis cannot be confirmed since the trough is currently buried at an elevation of -7/8 km. Interpretations of the available seismic data in the area are difficult and associated with high uncertainties (*Pfiffner et al.*, 1997; *Diehl et al.*, 2021). Additionally, as also stated in the result sections, the structures formed during and after this time interval, remain inaccessible to surface observations (see Figure 2). Consequently, the thrusts and reverse faults can be inferred primarily from large-scale seismic profiles (NFP20; *Pfiffner et al.*, 1997) and 3D tomographic imaging (*Diehl et al.*, 2021). This inevitably introduces some uncertainty into the proposed 4D reconstruction and structural model. In this context, alternative structural solutions remain possible, given the limited resolution of the deep geophysical datasets.

The cumulative vertical uplift between 22 and 10 Ma led to a significant uplift of the Aar Massif. This uplift also caused passive bending of the overlying, already-emplaced Helvetic nappe stack, as demonstrated by the deformation of major basal thrusts such as the Glarus and Doldenhorn thrusts (e.g., *Herwegh and Pfiffner*, 2005; *Pfiffner et al.*, 2011; *Musso Piantelli et al.*, 2022). The reconstruction shows that at 10 Ma the central regions of the structural half dome of the Aar Massif basement reached the topographic surface. In contrast, basement of the western and eastern massif sides was not exposed and still situated at an elevation of -2/3 km. Simultaneously, dextral strike-slip reactivation of the reverse faults was initiated in the south western region of the massif (green lines Figure 7d,e), as well as along the Rhone Simplon transtensional system (purple line in Figure 7d,e; *Grosjean et al.*, 2004; *Campani et al.*, 2014; *Cardello et al.*, 2024).

10 Ma to present (Figure 10d, e): The final phase of deformation was characterised by the development of a prominent NW-directed thrust structure, which forced a passive "en bloc" uplift of the Aar Massif (*Herwegh et al.*, 2017; *Nibourel et al.*, 2021a). During this phase, exhumation, which had previously been influenced by the interplay between isostasy and the orogenic stress field, became increasingly controlled by far-field compressional forces. In other words, thrusting ('horizontal tectonics') overtook the previously observed 'vertical tectonics' as the role of isostatic forces diminished (*Schlunegger and Kissling*, 2015; *Herwegh et al.*, 2020). Consequently, the exhumation rate diminished to lower values, decreasing from 0.4 mm/yr in the east to 0.2 in the west (Figure 7b). On the other hand, the shortening rates increased with higher shortening rates at the sides of the massif (0.85 to 1 mm/yr) and lower rates in the central regions of the massif (0.67 to 0.75 mm/yr). Simultaneously, compressional deformation along the northern front of the massif proceeded towards the North Alpine Foreland, where new north-northwest-vergent crustal ramps/thrusts were activated. This suggests a kinematic link of these thrusts with imbricate thrusting in the Subalpine Molasse (*Mock et al.*, 2020; *von Hagke et al.*, 2012). Moreover, also during this phase, strike-slip reactivation of reverse fault structures and potentially related motion of the Rhône-Simplon System continued to dissect the south western region of the massif (*Grosjean et al.*, 2004; *Campani et al.*, 2014; *Cardello et al.*, 2024; *Wehrens et al.*, 2016, 2017).

5.4 The Interplay Between Inherited Crustal Structures, and Deep Crustal Tectonics

From a geodynamic point of view, the External Crystalline Massifs of the European Alps provide an opportunity to study the kinematics, timing, and driving forces of exhumation processes during the inversion of passive margins during continent-continent collision (*Lacombe and Bellahsen*, 2016; *Herwegh et al.*, 2024). The geometry of the Aar Massif results from an interplay between deep crustal collisional tectonics and inherited structural configuration.

On one hand, as suggested by the buoyancy-driven model of *Herwegh et al.* (2017) and lithospheric mantle

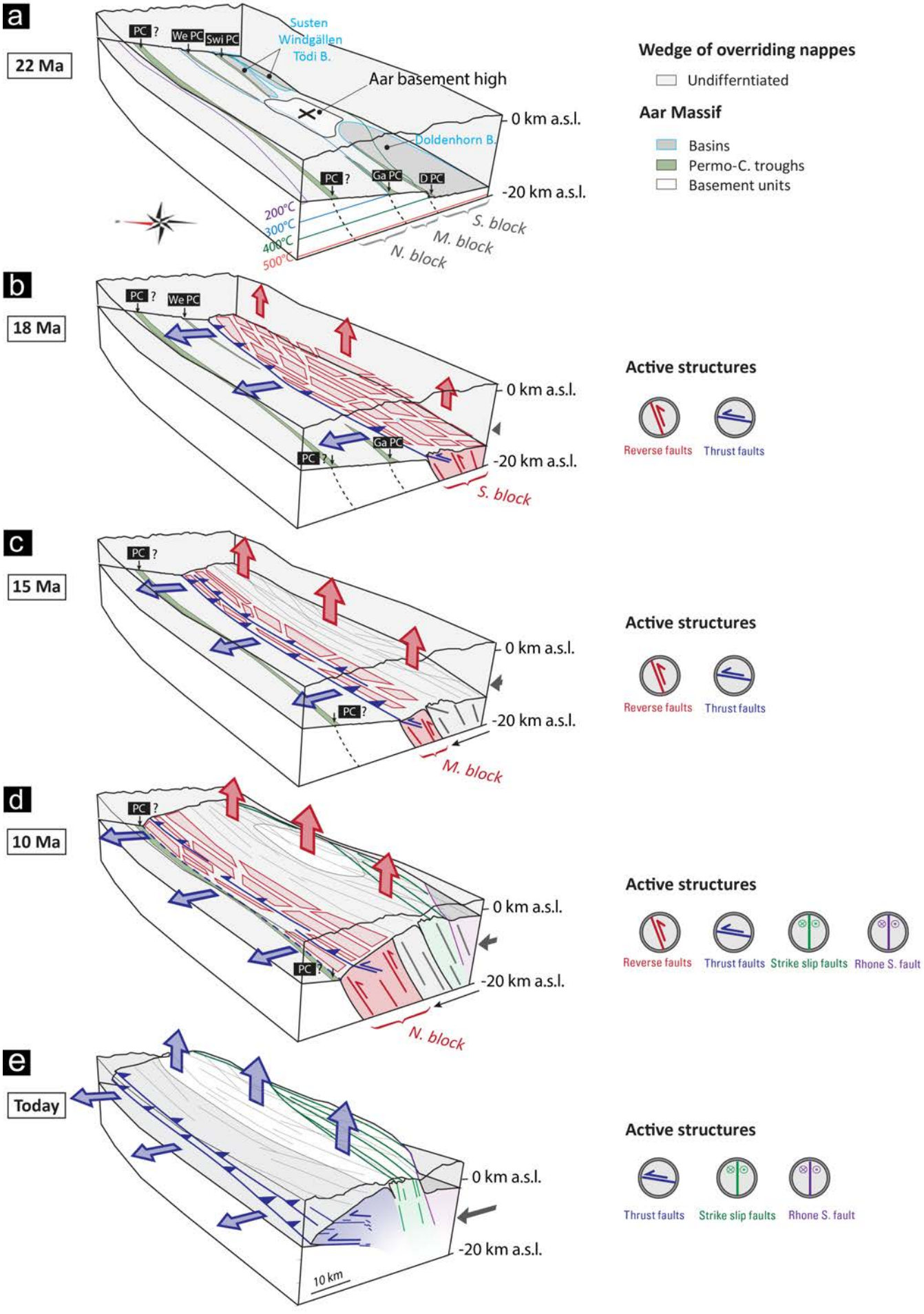
a
22 Ma
PC ?
We PC
Swi PC
Susten
Windgällen
Tödi B.
Aar basement high
0 km a.s.l.
Doldenhorn B.
PC ?
Ga PC
D PC
-20 km a.s.l.
200°C
300°C
400°C
500°C
S. block
M. block
N. block
Wedge of overriding nappes
Undifferntiated
Aar Massif
Basins
Permo-C. troughs
Basement units
b
18 Ma
PC ?
We PC
0 km a.s.l.
Ga PC
PC ?
-20 km a.s.l.
S. block
Active structures
Reverse faults
Thrust faults
c
15 Ma
PC ?
0 km a.s.l.
PC ?
-20 km a.s.l.
M. block
Active structures
Reverse faults
Thrust faults
d
10 Ma
PC ?
0 km a.s.l.
PC ?
-20 km a.s.l.
N. block
Active structures
Reverse faults
Thrust faults
Strike slip faults
Rhone S. fault
e
Today
0 km a.s.l.
-20 km a.s.l.
10 km
Active structures
Thrust faults
Strike slip faults
Rhone S. fault

Figure 10 – 4D geodynamic evolution of the Aar Massif during the late-stage Alpine orogeny. The figure shows a sketched version of the 4D model developed in this study. Abbreviations are listed in the figure captions of Figures 1 and 2. **(A)** At 22 Ma, the margin is buried at a depth ranging between -8 and -18 km with a horizontal gradient of 26°C/km. **(B)** At 18 Ma, the southern block of the massif is exhumed with reverse faults (forming rhomboidal blocks) and thrust faults localised at the front of the block. Greater shortening and exhumation in the central units accentuate the inherited height difference between the sides and the centre of the massif. **(C)** Exhumation migrates to the central block of the massif. Diffuse reverse faulting in the central block overprints and rotates the thrust structures formed previously in the southern block. New thrust fault structures were localised at the front of the central block. **(D)** Strong vertical exhumation of the northern block of the massif until 10 Ma forming the steep northern front of the massif. The central regions of the massif reached the surface and started to be eroded. **(E)** Between 10 Ma and the present day, large-scale thrust structures displace the northern block of the massif, causing an 'en bloc' exhumation of the basement units (*Nibourel et al.*, 2021b). Contemporaneously, from ca. 15 Ma, reverse faults in the south-western units of the massif were reactivated as strike-slip/oblique structures (green lines). The Rhone-Simplon fault (purple) was also active, displacing the southern margin of the massif.

rollback (*Schlunegger and Kissling*, 2015), the Aar Massif at 22 Ma underwent delamination, interpreted as a mechanical decoupling of the light continental upper and middle crust from the denser lower crust and lithospheric mantle (*Herwegh et al.*, 2017). As a result of this delamination, the gravitational slab-pull and negatively buoyant forces exerted by the European lithospheric mantle, which counterbalance the positively buoyant forces of the less dense upper and middle crust and the overlying rocks of the accretionary complex, were reduced (*Herwegh et al.*, 2017). This reduction in restraining forces allowed positive buoyancy to trigger the formation of steep to sub-vertical reverse faults with a strong rock uplift component (*Herwegh et al.*, 2017, 2024). These reverse faults formed pervasively within the basement and mostly did not reactivate inherited crustal extensional structures. Differences in crustal thickness therefore produced corresponding differences in buoyancy forces. The thicker and less stretched crust in the central regions of the massif (Aar Massif basement high), recorded a stronger exhumation component, compared to the W- and E-sides.

On the other hand, inherited shallow crustal Permo-Carboniferous troughs strongly controlled the position of Mesozoic normal faults and hence the development of the paleo-topography and basin asymmetries highlighted in Figure 9. During the Alpine inversion, new thrusts and reverse faults formed in the grabens/basins/throughs filled with Permo-Carboniferous and Mesozoic sediments. The pre-existing normal faults were not, or only weakly reactivated as described with field data by *Nibourel et al.* (2021a). A primary reason for this was their unfavourable orientation at the onset of reverse faulting (22 Ma), when the top of the basement dipped 10–15° southward, causing the normal faults to be in a subvertical position. In addition, the thermal and burial conditions strongly influenced the potential reactivation of inherited crustal structures. High metamorphic temperatures and significant tectonic burial tend to inhibit the reactivation of inherited crustal structures, as supported by numerical models (*Lafosse et al.*, 2016). At temperatures exceeding 300°C, such as those prevailing during the formation of the reverse faults, deformation is accommodated through the pervasive localisation of new structures, without significant reactivation of older ones. In contrast, at lower temperatures (<300°C), either reactivation of pre-existing faults or the localisation of newly formed ones is more likely, as for the case of the Permo-Carboniferous troughs (*Lafosse et al.*, 2016).

5.5 The Value of Large-scale 3D Geological Models

The case of the Aar Massif highlights the importance and value of integrating regional-scale 3D geological models when investigating complex geological systems, such as an orogen. These models enable the broadening of individual cross-sectional interpretations into the third dimension, allowing all available geological and geophysical constraints to be synthesised into a single geological model of the entire massif. This approach permitted to unravel the massif's along-strike variability, thereby providing resolution into the three-dimensional evolution and dynamics of such system. Moreover, large-scale 3D geological modelling of the 3D network of structures and lithostratigraphic contacts of mountain ranges has the potential to open the doors to a wide range of applications.

In fact, such 3D models provide our society with strategic insights into the still largely unexplored subsurface for sustainable development of infrastructures and for regional assessment of primary resources. Furthermore, modelling large-scale 3D fault patterns is important for understanding the valley morphology evolution, distribution of natural hazards and meteoric water circulation in orogens. Indeed, as in the case of the valley of the Aletsch Glacier (central Aar Massif), faults initiated at deep crustal level, nowadays exposed on the surface, strongly dominate the valley morphology and distribution of natural hazards in present-day Alpine landscapes (*Musso Piantelli et al.*, 2023).

This may have very important implications for both the exploitation of thermal anomalies of orogenic geothermal systems by performing realistic numerical simulations (e.g., *Waber et al.*, 2017; *Schneeberger et al.*, 2017; *Diamond et al.*, 2018; *Wanner et al.*, 2019; *Alt-Epping et al.*, 2021), and the evaluation of the influence of meteoric water on the seismicity of regional faults (e.g., *Byerlee*, 1993; *Lin et al.*, 2003; *Claesson et al.*, 2004; *Hosono et al.*, 2020).

6 Conclusion

The 4D geodynamic reconstruction discussed in this contribution allowed us to quantitatively describe the geodynamic evolution of the Aar Massif during the late stage of the Alpine collision. The 3D half dome-shape of the Aar Massif (here a simplified visualization of the 3D model https://skfb.ly/pA8Qx) is the result of several preconditioning factors and tectonic dynamics that have shaped this complex in space and time. The main results of this study are summarised as follows:

i) The Aar Massif is the result of the inversion of former ~6000 km^2 of passive European continental margin. Reconstruction of the proximal margin has revealed an asymmetric architecture with local half-graben basins, on the western and eastern sides of the massif and an Aar Massif basement high in the central regions of the massif. The resulting structural relief developed in this stage formed 20% of the present-day half dome-shape of the basement-cover contact of the massif. This geometry was controlled by mostly SSE-vergent Paleozoic to Mesozoic normal faults bounding Permo-Carboniferous to Mesozoic grabens and half-grabens. Displacement variations along these normal faults created differential subsidence/accommodation space, which explains the present-day thickness variations along the strike of the Aar Massif's para- and autochthonous sedimentary units (Figures 1 and 2). The same normal faults separated the basement blocks (i.e., northern, central southern blocks) already during the passive margin evolution.

ii) Collisional reverse faulting, thrusting and the resulting uplift of the basement units first localised in the southern block of the massif, then gradually migrated to the northern front of the massif, in an in-sequence deformation style. Inherited along strike variations in the crustal thickness of the not uniformly stretched margin of the thickened lower plate induced corresponding differences in the magnitude of the buoyancy forces. This, as shown in our 4D reconstruction, resulted in a non-cylindrical deformation and exhumation of the massif, leading to a larger uplift component in the central regions of the massif and smaller uplift at the W and E-sides of the massif.

iii) The reconstruction proposed in this article highlights the importance of integrating 3D geological models when studying complex geological systems, such as orogens, to address their three-dimensional evolution and dynamics.

The case of the Aar Massif has shown how inversion of passive margins in continent-continent collision is controlled by inherited basement geometries and P-T conditions during the inversion. Our palaeographic and 4D geodynamic reconstruction could motivate future studies exploring the role of inherited passive margin structures and their variations in the orogen-parallel direction in other External Crystalline Massifs or orogenic settings. Enlarging the scale of such reconstructions will help to better understand and predict the tectonic evolution of the advanced-stage collisional mountain belts.

Acknowledgements

We acknowledge Petroleum Experts (Petex) for providing an academic version of Move™, licensed to the Institute of Geological Sciences of the University of Bern. T. Schmid is thanked for the extraction of rose diagram plots of the lineament orientations. C. Rosenberg is thanked for constructive discussion on an earlier version of this manuscript. The study was funded by the Federal Office of Topography of Switzerland as pilot study of the Swiss Alps 3D project (swisstopo; 570 300 4426 ARIWA 9101-01-Contract). We finally thank the Tektonika editors Chiara Montomoli and Robin Lacassin, as well as the two reviewers Salvatore Iaccarino and Philippe H. Leloup for their revisions.

Author contributions

MH and **AB** obtained the funding for this project. **FMP**, **MH** and **AB** designed the study. All authors carried out the fieldwork in the area in recent years. **FMP** made the retrodeformation and 3D modelling with additional scientific input from **MH**, **AB**, and **LN**. **LN** provided the paleo peak temperature dataset. **FMP** prepared the manuscript and figures with contribution from all co-authors. All authors read and approved the manuscript.

Data availability

All datasets used as input for the study and 3D geological model (see list in Chapter 2 of the Supporting Information) are publicly available via the swisstopo platforms at https://map.geo.admin.ch/ and https://shop.swisstopo.admin.ch/. The resulting 3D geological model can be visualized at the following links: https://skfb.ly/pA8Qx and https://viewer.swissgeol.ch/. The 3D geological model will be made available upon request.

Competing interests

The authors declare no competing interests.

Peer review

This publication was peer-reviewed by Salvatore Iaccarino and Philippe H. Leloup. The full peer-review report can be found here: Review Report.

Copyright notice

References

Abrecht, J. (1994), Geologic units of the Aar massif and their pre-Alpine rock associations: a critical review : The pre-Alpine crustal evolution of the Aar-, Gotthard- and Tavetsch massifs, *Schweizerische mineralogische und petrographische Mitteilungen*, *74*(1), 5–27.

Alt-Epping, P., L. W. Diamond, C. Wanner, and G. E. Hammond (2021), Effect of glacial/interglacial recharge conditions on flow of meteoric water through deep orogenic faults: Insights into the geothermal system at grimsel pass, Switzerland, *Journal of Geophysical Research. Solid Earth*, *126*(7), e2020JB021,271, https://doi.org/10.1029/2020jb021271.

Badertscher, N., and M. Burkhard (1998), Inversion alpine du graben Permo-Carbonifère de Salvan-Dorénaz et sa relation avec le chevauchement de la nappe de Morcles sus-jacente, *Eclogae Geologicae Helvetiae*, *91*, 359/373.

Ballèvre, M., P. Manzotti, and G. V. Dal Piaz (2018), Pre-alpine (variscan) inheritance: A key for the location of the future valaisan basin (western alps), *Tectonics*, *37*(3), 786–817, https://doi.org/10.1002/2017tc004633.

Balázs, A., E. Burov, L. Matenco, K. Vogt, T. Francois, and S. Cloetingh (2017), Symmetry during the syn- and post-rift evolution of extensional back-arc basins: The role of inherited orogenic structures, *Earth and Planetary Science Letters*, *462*, 86–98, https://doi.org/10.1016/j.epsl.2017.01.015.

Bambauer, H. U., M. Herwegh, and H. Kroll (2009), Quartz as indicator mineral in the Central Swiss Alps: the quartz recrystallization isograd in the rock series of the northern Aar massif, *Swiss Journal of Geosciences*, *102*(2), 345–351, https://doi.org/10.1007/s00015-009-1319-z.

Baumberger, R., M. Herwegh, and E. Kissling (2022), Remote sensing and field data based structural 3D modelling (haslital, Switzerland) in combination with uncertainty estimation and verification by underground data, https://doi.org/10.1002/9781119313922.ch10.

Bauville, A., and S. M. Schmalholz (2015), Transition from thin- to thick-skinned tectonics and consequences for nappe formation: Numerical simulations and applications to the Helvetic nappe system, Switzerland, *Tectonophysics*, *665*, 101–117, https://doi.org/10.1016/j.tecto.2015.09.030.

Bauville, A., and S. M. Schmalholz (2017), Tectonic inheritance and kinematic strain localization as trigger for the formation of the Helvetic nappes, Switzerland, *Swiss Journal of Geosciences*, *110*(2), 523–534, https://doi.org/10.1007/s00015-017-0260-9.

Beaumont, C., J. A. Muñoz, J. Hamilton, and P. Fullsack (2000), Factors controlling the Alpine evolution of the central Pyrenees inferred from a comparison of observations and geodynamical models, *Journal of Geophysical Research*, *105*(B4), 8121–8145, https://doi.org/10.1029/1999jb900390.

Bellahsen, N., L. Jolivet, O. Lacombe, M. Bellanger, A. Boutoux, S. Garcia, F. Mouthereau, L. Le Pourhiet, and C. Gumiaux (2012), Mechanisms of margin inversion in the external Western Alps: Implications for crustal rheology, *Tectonophysics*, *560-561*, 62–83, https://doi.org/10.1016/j.tecto.2012.06.022.

Bellahsen, N., F. Mouthereau, A. Boutoux, M. Bellanger, O. Lacombe, L. Jolivet, and Y. Rolland (2014), Collision kinematics in the western external Alps: Kinematics of the Alpine collision, *Tectonics*, *33*(6), 1055–1088, https://doi.org/10.1002/2013tc003453.

Bellanger, M., N. Bellahsen, L. Jolivet, T. Baudin, R. Augier, and A. Boutoux (2014), Basement shear zones development and shortening kinematics in the Ecrins Massif, Western Alps, *Tectonics*, *33*(2), 84–111, https://doi.org/10.1002/2013tc003294.

Bergemann, C., E. Gnos, A. Berger, M. Whitehouse, J. Mullis, P. Wehrens, T. Pettke, and E. Janots (2017), Th-Pb ion probe dating of zoned hydrothermal monazite and its implications for repeated shear zone activity: An example from the Central Alps, Switzerland: Dating Hydrothermal Monazite, Shear Zones, *Tectonics*, *36*(4), 671–689, https://doi.org/10.1002/2016tc004407.

Berger, A., I. Mercolli, and M. Herwegh (2017a), Geological Map of the Aar Massif, Tavetsch and Gotthard Nappes.

Berger, A., P. Wehrens, P. Lanari, H. Zwingmann, and M. Herwegh (2017b), Microstructures, mineral chemistry and geochronology of white micas along a retrograde evolution: An example from the Aar massif (Central Alps, Switzerland), *Tectonophysics*, *721*, 179–195, https://doi.org/10.1016/j.tecto.2017.09.019.

Berger, A., M. Engi, S. Erne-Schmid, C. Glotzbach, C. Spiegel, R. de Goede, and M. Herwegh (2020), The relation between peak metamorphic temperatures and subsequent cooling during continent–continent collision (western Central Alps, Switzerland), *Swiss Journal of Geosciences*, *113*(1), 4, https://doi.org/10.1186/s00015-020-00356-4.

Beyssac, O., M. Simoes, J. P. Avouac, K. A. Farley, Y.-G. Chen, Y.-C. Chan, and B. Goffé (2007), Late Cenozoic metamorphic evolution and exhumation of Taiwan: EXHUMATION OF THE TAIWAN MOUNTAIN BELT, *Tectonics*, *26*(6), https://doi.org/10.1029/2006tc002064.

Boutoux, A., N. Bellahsen, O. Lacombe, A. Verlaguet, and F. Mouthereau (2014), Inversion of pre-orogenic extensional basins in the external Western Alps: Structure, microstructures and restoration, *Journal of Structural Geology*, *60*, 13–29, https://doi.org/10.1016/j.jsg.2013.12.014.

Boutoux, A., N. Bellahsen, U. Nanni, R. Pik, A. Verlaguet, Y. Rolland, and O. Lacombe (2016), Thermal and structural evolution of the external Western Alps: Insights from (U–Th–Sm)/He thermochronology and RSCM thermometry in the Aiguilles Rouges/Mont Blanc massifs, *Tectonophysics*, *683*, 109–123, https://doi.org/10.1016/j.tecto.2016.06.010.

Brisson, S., F. Wellmann, N. Chudalla, J. von Harten, and C. von Hagke (2023), Estimating uncertainties in 3-D models of complex fold-and-thrust belts: A case study of the Eastern Alps triangle zone, *Applied Computing and Geosciences*, *18*(100115), 100,115, https://doi.org/10.1016/j.acags.2023.100115.

Burkhard, M. (1988), L'Helvétique de la bordure occidentale du massif de l'Aar (évolution tectonique et métamorphique), *Eclogae geologicae Helvetiae*, *81*(1), 63–114.

Butler, R. W. H., E. Tavarnelli, and M. Grasso (2006), Structural inheritance in mountain belts: An Alpine–Apennine perspective, *Journal of Structural Geology*, *28*(11), 1893–1908, https://doi.org/10.1016/j.jsg.2006.09.006.

Byerlee, J. (1993), Model for episodic flow of high-pressure water in fault zones before earthquakes, *Geology*, *21*(4), 303, https://doi.org/10.1130/0091-7613(1993)021<0303:mfefoh>2.3.co;2.

Campani, M., A. Mulch, O. Kempf, F. Schlunegger, and N. Mancktelow (2012), Miocene paleotopography of the central alps, *Earth and Planetary Science Letters*, *337-338*, 174–185, https://doi.org/10.1016/j.epsl.2012.05.017.

Campani, M., N. Mancktelow, and G. Courrioux (2014), The 3D interplay between folding and faulting in a syn-orogenic extensional system: the Simplon Fault Zone in the Central Alps (Switzerland and Italy), *Swiss Journal of Geosciences*, *107*(2-3), 251–271, https://doi.org/10.1007/s00015-014-0163-y.

Cardello, G. L., and N. S. Mancktelow (2014), Cretaceous syn-sedimentary faulting in the Wildhorn Nappe (SW Switzerland), *Swiss Journal of Geosciences*, *107*(2-3), 223–250, https://doi.org/10.1007/s00015-014-0166-8.

Cardello, G. L., S. M. Bernasconi, M. G. Fellin, M. Rahn, R. Rosskopf, C. Maden, and N. S. Mancktelow (2024), Carbonate deformation through the brittle-ductile transition: The case of the SW Helvetic nappes, Switzerland, *Journal of Structural Geology*, *181*(105083), 105,083, https://doi.org/10.1016/j.jsg.2024.105083.

Challandes, N., D. Marquer, and I. M. Villa (2008), P-T-t modelling, fluid circulation, and 39Ar-40Ar and Rb-Sr mica ages in the Aar Massif shear zones (Swiss Alps), *Swiss Journal of Geosciences*, *101*(2), 269–288, https://doi.org/10.1007/s00015-008-1260-6.

Choukroune, P., and D. Gapais (1983), Strain pattern in the Aar Granite (Central Alps): Orthogneiss developed by bulk inhomogeneous flattening, *Journal of Structural Geology*, *5*(3-4), 411–418, https://doi.org/10.1016/0191-8141(83)90027-5.

Claesson, L., A. Skelton, C. Graham, C. Dietl, M. Mörth, P. Torssander, and I. Kockum (2004), Hydrogeochemical changes before and after a major earthquake, *Geology*, *32*(8), 641–644, https://doi.org/10.1130/G20542.1.

Collet, L. W. (1947), La géologie du versant sud du massif de Gaster, *Eclogae Geologicae Helvetiae*, *40*(2), 257–281.

Corti, G., J. van Wijk, S. Cloetingh, and C. K. Morley (2007), Tectonic inheritance and continental rift architecture: Numerical and analogue models of the East African Rift system: INHERITANCE AND RIFT ARCHITECTURE, *Tectonics*, *26*(6), https://doi.org/10.1029/2006tc002086.

Diamond, L. W., C. Wanner, and H. N. Waber (2018), Penetration depth of meteoric water in orogenic geothermal systems, *Geology*, *46*(12), 1063–1066, https://doi.org/10.1130/G45394.1.

Diehl, T., E. Kissling, M. Herwegh, and S. M. Schmid (2021), Improving absolute hypocenter accuracy with 3D*pg*and*Sgbody*-wave inversion procedures and application to earthquakes in the central alps region, *Journal of Geophysical Research. Solid Earth*, *126*(12), e2021JB022,155, https://doi.org/10.1029/2021jb022155.

Dolivo, E. (1982), Nouvelles observations structurales au SW du massif de l'Aar entre Visp et Gampel, *Matériaux pour la Carte Géologique de la Suisse, n.s.*, *157*.

Ebert, A., M. Herwegh, A. Berger, and A. Pfiffner (2008), Grain coarsening maps for polymineralic carbonate mylonites: A calibration based on data from different Helvetic nappes (Switzerland), *Tectonophysics*, *457*(3-4), 128–142, https://doi.org/10.1016/j.tecto.2008.05.007.

Egli, D., and N. Mancktelow (2013), The structural history of the Mont Blanc massif with regard to models for its recent exhumation, *Swiss Journal of Geosciences*, *106*(3), 469–489, https://doi.org/10.1007/s00015-013-0153-5.

Frey, M., M. Teichmueller, R. Teichmueller, J. Mullis, B. Kuenzi, A. Breitschmid, U. Gruner, and B. Schwizer (1980), Very low grade metamorphism in external parts of the Central Alps: illite crystallinity, coal rank and fluid inclusion data, *Eclogae Geologicae Helvetiae*, *73*(1), 173–203.

Frings, K., C. von Hagke, F. Wellman, E. Heim, M. de la Varga, H. Ortner, and E. Luijendik (2023), Constraining the 3-D geometry of fold-thrust belts using section balancing vs. 3-D interpolative structural and probabilistic modeling, *Tektonika*, *1*(2), https://doi.org/10.55575/tektonika2023.1.2.21.

Froitzheim, N., S. M. Schmid, and M. Frey (1996), Mesozoic paleogeography and the timing of eclogite-facies metamorphism in the Alps : a working hypothesis, *Eclogae Geologicae Helvetiae*, *89*(1), 81, https://doi.org/10.5169/SEALS-167895.

Girault, J. B., N. Bellahsen, A. Boutoux, C. L. Rosenberg, U. Nanni, A. Verlaguet, and O. Beyssac (2020), The 3-D thermal structure of the helvetic nappes of the European alps: Implications for collisional processes, *Tectonics*, *39*(3), e2018TC005,334, https://doi.org/10.1029/2018tc005334.

Girault, J. B., N. Bellahsen, M. Bernet, R. Pik, N. Loget, E. Lasseur, C. L. Rosenberg, M. Balvay, and M. Sonnet (2022), Exhumation of the Western Alpine collisional wedge: New thermochronological data, *Tectonophysics*, *822*(229155), 229,155, https://doi.org/10.1016/j.tecto.2021.229155.

Gisler, C., P. A. Hochuli, K. Ramseyer, H. Bläsi, and F. Schlunegger (2007), Sedimentological and palynological constraints on the basal Triassic sequence in Central Switzerland, *Swiss Journal of Geosciences*, *100*(2), 263–272, https://doi.org/10.1007/s00015-007-1225-1.

Glotzbach, C., J. Reinecker, M. Danišík, M. Rahn, W. Frisch, and C. Spiegel (2010), Thermal history of the central Gotthard and Aar massifs, European Alps: Evidence for steady state, long-term exhumation, *Journal of Geophysical Research*, *115*(F3), https://doi.org/10.1029/2009jf001304.

Goncalves, P., E. Oliot, D. Marquer, and J. A. D. Connolly (2012), Role of chemical processes on shear zone formation: an example from the Grimsel metagranodiorite (Aar massif, Central Alps): SHEAR ZONE FORMATION, *Journal of Metamorphic Geology*, *30*(7), 703–722, https://doi.org/10.1111/j.1525-1314.2012.00991.x.

Granado, P., and J. B. Ruh (2019), Numerical modelling of inversion tectonics in fold-and-thrust belts, *Tectonophysics*, *763*, 14–29, https://doi.org/10.1016/j.tecto.2019.04.033.

Grosjean, G., C. Sue, and M. Burkhard (2004), Late Neogene extension in the vicinity of the Simplon fault zone (central Alps, Switzerland), *Eclogae geologicae Helvetiae*, *97*(1), 33–46, https://doi.org/10.1007/s00015-004-1114-9.

Günzler-Seiffert, H. (1952), Alte Brüche im Kreide/Tertiär-Anteil der Wildhorndecke Zwischen Rhone und Rhein, *Geologische Rundschau*, *40*(2), 211–239, https://doi.org/10.1007/bf01803434.

Handy, M. R., S. M. Schmid, R. Bousquet, E. Kissling, and D. Bernoulli (2010), Reconciling plate-tectonic reconstructions of Alpine Tethys with the geological–geophysical record of spreading and subduction in the Alps, *Earth-Science Reviews*, *102*(3-4), 121–158, https://doi.org/10.1016/j.earscirev.2010.06.002.

Herwegh, M., and O. A. Pfiffner (2005), Tectono-metamorphic evolution of a nappe stack: A case study of the Swiss Alps, *Tectonophysics*, *404*(1-2), 55–76, https://doi.org/10.1016/j.tecto.2005.05.002.

Herwegh, M., A. Berger, R. Baumberger, P. Wehrens, and E. Kissling (2017), Large-scale crustal-block-extrusion during late alpine collision, *Scientific Reports*, *7*(1), 413, https://doi.org/10.1038/s41598-017-00440-0.

Herwegh, M., A. Berger, C. Glotzbach, C. Wangenheim, S. Mock, P. Wehrens, R. Baumberger, D. Egli, and E. Kissling (2020), Late stages of continent-continent collision: Timing, kinematic evolution, and exhumation of the Northern rim (Aar Massif) of the Alps, *Earth-Science Reviews*, *200*(102959), 102,959, https://doi.org/10.1016/j.earscirev.2019.102959.

Herwegh, M., A. Berger, N. Bellahsen, Y. Rolland, and E. Kissling (2024), Evolution of the external crystalline massifs of the European alps: From massif to lithosphere scale, https://doi.org/10.1002/9781394299560.ch2.

Hosono, T., C. Yamada, M. Manga, C.-Y. Wang, and M. Tanimizu (2020), Stable isotopes show that earthquakes enhance permeability and release water from mountains, *Nature Communications*, *11*(1), 2776, https://doi.org/10.1038/s41467-020-16604-y.

Hänni, R., and O.-A. Pfiffner (2001), Evolution and internal structure of the Helvetic nappes in the Bernese Oberland, *Eclogae geologicae Helvetiae*, *94*(2), 161–171, https://doi.org/10.7892/BORIS.86847.

Kempf, O., and O. Adrian Pfiffner (2004), Early Tertiary evolution of the North Alpine Foreland Basin of the Swiss Alps and adjoining areas, *Basin Research*, *16*(4), 549–567, https://doi.org/10.1111/j.1365-2117.2004.00246.x.

Kissling, E., and F. Schlunegger (2018), Rollback Orogeny Model for the Evolution of the Swiss Alps, *Tectonics*, *37*(4), 1097–1115, https://doi.org/10.1002/2017TC004762.

Krayenbuhl, T., and A. Steck (2009), Structure and kinematics of the Jungfrau syncline, Faflertal (Valais, Alps), and its regional significance, *Swiss Journal of Geosciences*, *102*(3), 441–456, https://doi.org/10.1007/s00015-009-1333-1.

Krebs, J. (1925), Geologische Beschreibung der Blümlisalp Gruppe, *Tech. rep.*, Swisstopo.

Lacombe, O., and N. Bellahsen (2016), Thick-skinned tectonics and basement-involved fold–thrust belts: insights from selected Cenozoic orogens, *Geological Magazine*, *153*(5-6), 763–810, https://doi.org/10.1017/s0016756816000078.

Lacombe, O., and F. Mouthereau (2002), Basement-involved shortening and deep detachment tectonics in forelands of orogens: Insights from recent collision belts (Taiwan, Western Alps, Pyrenees): BASEMENT-INVOLVED SHORTENING IN FORELANDS, *Tectonics*, *21*(4), 12–1–12–22, https://doi.org/10.1029/2001tc901018.

Lafosse, M., A. Boutoux, N. Bellahsen, and L. Le Pourhiet (2016), Role of tectonic burial and temperature on the inversion of inherited extensional basins during collision, *Geological Magazine*, *153*(5-6), 811–826, https://doi.org/10.1017/s0016756816000510.

Leloup, P. H., N. Arnaud, E. R. Sobel, and R. Lacassin (2005), Alpine thermal and structural evolution of the highest external crystalline massif: The Mont Blanc, *Tectonics*, *24*(4), https://doi.org/10.1029/2004TC001676.

Lin, A., N. Tanaka, S. Uda, and M. Satish-Kumar (2003), Repeated coseismic infiltration of meteoric and seawater into deep fault zones: a case study of the Nojima fault zone, Japan, *Chemical Geology*, *202*(1-2), 139–153, https://doi.org/10.1016/j.chemgeo.2003.08.010.

Mair, D., A. Lechmann, M. Herwegh, L. Nibourel, and F. Schlunegger (2018), Linking Alpine deformation in the Aar Massif basement and its cover units – the case of the Jungfrau–Eiger mountains (Central Alps, Switzerland), *Solid Earth*, *9*(5), 1099–1122, https://doi.org/10.5194/se-9-1099-2018.

Mancktelow, N. (1985), The Simplon line: a major displacement zone in the western Lepontine Alps, *Eclogae geologicae Helvetiae*, *78*(1), 73–96.

Mart, Y., and O. Dauteuil (2000), Analogue experiments of propagation of oblique rifts, *Tectonophysics*, *316*(1-2), 121–132, https://doi.org/10.1016/s0040-1951(99)00231-0.

Masini, E., G. Manatschal, and G. Mohn (2013), The Alpine Tethys rifted margins: Reconciling old and new ideas to understand the stratigraphic architecture of magma-poor rifted margins, *Sedimentology*, *60*(1), 174–196, https://doi.org/10.1111/sed.12017.

Masson, H., R. Herb, and A. Steck (1980), Helvetic Alps of Western Switzerland, Excusion no. 1, *Geology of Switzerland–a guide book, Part B, Geological Excursions, edited by: Trümpy*, pp. 109–153.

McClay, K. R., and M. J. White (1995), Analogue modelling of orthogonal and oblique rifting, *Marine and Petroleum*

Geology, *12*(2), 137–151, https://doi.org/10.1016/0264-8172(95)92835-k.

Mercier, A., P. H. Leloup, G. Courrioux, S. Caritg, S. Lopez, P. Grandjean, S. Passot, and A. Kalifi (2023), Large thrusting and late faulting shape the Aiguilles Rouges crystalline massif (Western Alps), structural implications, *Tectonophysics*, *847*(229691), 229,691, https://doi.org/10.1016/j.tecto.2022.229691.

Michalski, I., and M. Soom (1990), The Alpine thermo-tectonic evolution of the Aar and Gotthard massifs, central Switzerland: Fission track ages on zircon and apatite and K-Ar mica ages, *Schweizerische mineralogische und petrographische Mitteilungen*.

Mock, S. (2014), Deformation of the Sediment-Crystalline Contact in the Northern Aar Massif (Innertkirchen, Bernese Oberland), Master's thesis, University of Bern, Bern, Switzerland.

Mock, S., C. von Hagke, F. Schlunegger, I. Dunkl, and M. Herwegh (2020), Long-wavelength late-Miocene thrusting in the north Alpine foreland: implications for late orogenic processes, *Solid Earth*, *11*(5), 1823–1847, https://doi.org/10.5194/se-11-1823-2020.

Mohn, G., G. Manatschal, E. Masini, and O. Müntener (2011), Rift-related inheritance in orogens: a case study from the Austroalpine nappes in Central Alps (SE-Switzerland and N-Italy), *International Journal of Earth Sciences*, *100*(5), 937–961, https://doi.org/10.1007/s00531-010-0630-2.

Mohn, G., G. Manatschal, M. Beltrando, E. Masini, and N. Kusznir (2012), Necking of continental crust in magma-poor rifted margins: Evidence from the fossil Alpine Tethys margins: NECKING OF CONTINENTAL CRUST, *Tectonics*, *31*(1), TC1012, https://doi.org/10.1029/2011tc002961.

Mouthereau, F., A. B. Watts, and E. Burov (2013), Structure of orogenic belts controlled by lithosphere age, *Nature Geoscience*, *6*(9), 785–789, https://doi.org/10.1038/ngeo1902.

Musso Piantelli, F., D. Mair, A. Berger, F. Schlunegger, M. Wiederkehr, E. Kurmann, R. Baumberger, A. Möri, and M. Herwegh (2022), 4D reconstruction of the Doldenhorn nappe-basement system in the Aar massif: Insights into late-stage continent-continent collision in the Swiss Alps, *Tectonophysics*, *843*(229586), 229,586, https://doi.org/10.1016/j.tecto.2022.229586.

Musso Piantelli, F., S. Truttmann, and M. Herwegh (2023), The control of collisional tectonics over valley morphology: the case of the largest glacier in the European Alps, *Terra nova*, *35*(5), 424–431, https://doi.org/10.1111/ter.12666.

Muñoz, J. A. (1992), Evolution of a continental collision belt: ECORS-Pyrenees crustal balanced cross-section, in *Thrust Tectonics*, edited by K. R. McClay, pp. 235–246, Springer Netherlands, Dordrecht, https://doi.org/10.1007/978-94-011-3066-0_21.

Nibourel, L., A. Berger, D. Egli, N. K. Luensdorf, and M. Herwegh (2018), Large vertical displacements of a crystalline massif recorded by Raman thermometry, *Geology*, *46*(10), 879–882, https://doi.org/10.1130/g45121.1.

Nibourel, L., A. Berger, D. Egli, S. Heuberger, and M. Herwegh (2021a), Structural and thermal evolution of the eastern Aar Massif: insights from structural field work and Raman thermometry, *Swiss Journal of Geosciences*, *114*(1), 9, https://doi.org/10.1186/s00015-020-00381-3.

Nibourel, L., M. Rahn, I. Dunkl, A. Berger, F. Herman, T. Diehl, S. Heuberger, and M. Herwegh (2021b), Orogen-parallel migration of exhumation in the Eastern aar massif revealed by low-T thermochronometry, *Journal of Geophysical Research. Solid Earth*, *126*(10), e2020JB020,799, https://doi.org/10.1029/2020jb020799.

Peron-Pinvidic, G., G. Manatschal, and P. T. Osmundsen (2013), Structural comparison of archetypal Atlantic rifted margins: A review of observations and concepts, *Marine and Petroleum Geology*, *43*, 21–47, https://doi.org/10.1016/j.marpetgeo.2013.02.002.

Pfiffner, A. O., P. Lehner, P. Heitzmann, S. Mueller, and A. Steck (1997), *Deep structure of the Swiss alps: Results of NRP 20*, 1995 ed., Springer, Basel, Switzerland.

Pfiffner, O., M. Burkhard, R. Hänni, A. Kammer, R. Kligfield, N. Mancktelow, J. Menkveld, J. Ramsay, S. Schmid, and R. Zurbriggen (2011), Structural map of the Helvetic zone of the Swiss Alps, including Vorarlberg (Austria) and Haute Savoie (France), in *Geological Special Map 128/1-7*, Bundesamt für Landestopografie swisstopo, Switzerland.

Pfiffner, O. A. (2006), Thick-skinned and thin-skinned styles of continental contraction, in *Styles of Continental Contraction*, pp. 153–177, Geological Society of America, https://doi.org/10.1130/2006.2414(09).

Pfiffner, O. A. (2024), *Geologie der Alpen*, vol. 8416, 2 ed., UTB, Stuttgart, Germany.

Rahn, M. K., and B. Grasemann (1999), Fission track and numerical thermal modeling of differential exhumation of the Glarus thrust plane (Switzerland), *Earth and Planetary Science Letters*, *169*(3-4), 245–259, https://doi.org/10.1016/s0012-821x(99)00078-3.

Ricchi, E., C. A. Bergemann, E. Gnos, A. Berger, D. Rubatto, and M. J. Whitehouse (2019), Constraining deformation phases in the Aar Massif and the Gotthard Nappe (Switzerland) using Th-Pb crystallization ages of fissure monazite-(Ce), *Lithos*, *342-343*, 223–238, https://doi.org/10.1016/j.lithos.2019.04.014.

Rohr, K. (1926), Stratigraphische und tektonische Untersuchung der Zwischenbildungen am Nordrand des Aarmassivs (zwischen Wendenjoch und Wetterhorn), *Tech. rep.*, Bern.

Rolland, Y., S. F. Cox, and M. Corsini (2009), Constraining deformation stages in brittle–ductile shear zones from combined field mapping and 40Ar/39Ar dating: The structural evolution of the Grimsel Pass area (Aar Massif, Swiss Alps), *Journal of Structural Geology*, *31*(11), 1377–1394, https://doi.org/10.1016/j.jsg.2009.08.003.

Rosenberg, C. L., and E. Kissling (2013), Three-dimensional insight into Central-Alpine collision: Lower-plate or upper-plate indentation?, *Geology*, *41*(12), 1219–1222, https://doi.org/10.1130/G34584.1.

Rosenberg, C. L., A. Berger, N. Bellahsen, and R. Bousquet (2015), Relating orogen width to shortening, erosion, and exhumation during Alpine collision: ALPINE WIDTH AND COLLISIONAL SHORTENING, *Tectonics*, *34*(6), 1306–1328, https://doi.org/10.1002/2014tc003736.

Rosenberg, C. L., N. Bellahsen, A. Rabaute, and J.-B. Girault (2021), Distribution, style, amount of collisional shortening, and their link to Barrovian metamorphism in the European Alps, *Earth-Science Reviews*, *222*(103774), 103,774, https://doi.org/10.1016/j.earscirev.2021.103774.

Santantonio, M., and E. Carminati (2011), Jurassic rifting evolution of the Apennines and Southern Alps (Italy): Parallels and differences, *Geological Society of America Bulletin*, *123*(3-4), 468–484, https://doi.org/10.1130/B30104.1.

Schlunegger, F., and E. Kissling (2015), Slab rollback orogeny in the Alps and evolution of the Swiss Molasse basin, *Nature Communications*, *6*(1), 8605, https://doi.org/10.1038/ncomms9605.

Schmid, S. M., O. A. Pfiffner, N. Froitzheim, G. Schönborn, and E. Kissling (1996), Geophysical-geological transect and tectonic evolution of the Swiss-Italian Alps, *Tectonics*, *15*(5), 1036–1064, https://doi.org/10.1029/96tc00433.

Schmid, S. M., B. Fügenschuh, E. Kissling, and R. Schuster (2004), Tectonic map and overall architecture of the Alpine orogen, *Eclogae geologicae Helvetiae*, *97*(1), 93–117, https://doi.org/10.1007/s00015-004-1113-x.

Schneeberger, R., M. de La Varga, D. Egli, A. Berger, F. Kober, F. Wellmann, and M. Herwegh (2017), Methods and uncertainty estimations of 3-D structural modelling in crystalline rocks: a case study, *Solid Earth*, *8*(5), 987–1002, https://doi.org/10.5194/se-8-987-2017.

Shi, Y., and C.-Y. Wang (1987), Two-dimensional modeling of the P-T-t paths of regional metamorphism in simple overthrust terrains, *Geology*, *15*(11), 1048, https://doi.org/10.1130/0091-7613(1987)15<1048:tmotpp>2.0.co;2.

Sibson, R. H. (1977), Fault rocks and fault mechanisms, *Journal of the Geological Society*, *133*(3), 191–213, https://doi.org/10.1144/gsjgs.133.3.0191.

Spitz, R., A. Bauville, J.-L. Epard, B. J. P. Kaus, A. A. Popov, and S. M. Schmalholz (2020), Control of 3-D tectonic inheritance on fold-and-thrust belts: insights from 3-D numerical models and application to the Helvetic nappe system, *Solid Earth*, *11*(3), 999–1026, https://doi.org/10.5194/se-11-999-2020.

Steck, A. (1968), Die alpidischen Strukturen in den Zentralen Aaregraniten des westlichen Aarmassivs, *Eclogae geologicae Helvetiae*, *61*, 19–48, https://doi.org/10.5169/SEALS-163584.

Steck, A. (2008), Tectonics of the Simplon massif and Lepontine gneiss dome: deformation structures due to collision between the underthrusting European plate and the Adriatic indenter, *Swiss Journal of Geosciences*, *101*(2), 515–546, https://doi.org/10.1007/s00015-008-1283-z.

Strasser, A. (1982), Fazielle und sedimentologische Entwicklung des Betlis-Kalkes (Valanginian) im Helvetikum der Zentral-und Ostschweiz, *Eclogae Geologicae Helvetiae*, *75*, 1–21.

swisstopo (2024), Tectonic Map of Switzerland.

Tricart, P. (1984), From passive margin to continental collision; a tectonic scenario for the Western Alps, *American Journal of Science*, *284*(2), 97–120, https://doi.org/10.2475/ajs.284.2.97.

Trümpy, R. (1952), Der Nordrand der Liasischen Tethys in den Schweizer Alpen, *Geologische Rundschau*, *40*(2), 239–242, https://doi.org/10.1007/bf01803435.

Trümpy, R. (1980), *Geology of Switzerland: a guide book*, Wepf and Company, Basel.

Tugend, J., G. Manatschal, N. J. Kusznir, and E. Masini (2015), Characterizing and identifying structural domains at rifted continental margins: application to the Bay of Biscay margins and its Western Pyrenean fossil remnants, *Geological Society Special Publication*, *413*, 171–203, https://doi.org/10.1144/SP413.3.

Vergés, J., E. Saura, E. Casciello, M. Fernàndez, A. Villaseñor, I. Jiménez-Munt, and D. García-Castellanos (2011), Crustal-scale cross-sections across the NW Zagros belt: implications for the Arabian margin reconstruction, *Geological Magazine*, *148*(5-6), 739–761, https://doi.org/10.1017/s0016756811000331.

von Hagke, C., C. E. Cederbom, O. Oncken, D. F. Stöckli, M. K. Rahn, and F. Schlunegger (2012), Linking the northern Alps with their foreland: The latest exhumation history resolved by low-temperature thermochronology, *Tectonics*, *31*(5), TC5010, https://doi.org/10.1029/2011TC003078.

Waber, H. N., R. Schneeberger, U. K. Mäder, and C. Wanner (2017), Constraints on evolution and residence time of geothermal water in granitic rocks at grimsel (Switzerland), *Procedia Earth and Planetary Science*, *17*, 774–777, https://doi.org/10.1016/j.proeps.2017.01.026.

Wanner, C., L. W. Diamond, and P. Alt-Epping (2019), Quantification of 3-D thermal anomalies from surface observations of an orogenic geothermal system (Grimsel Pass, Swiss Alps), *Journal of Geophysical Research. Solid Earth*, *124*(11), 10,839–10,854, https://doi.org/10.1029/2019jb018335.

Wehrens, P., A. Berger, M. Peters, T. Spillmann, and M. Herwegh (2016), Deformation at the frictional-viscous transition: Evidence for cycles of fluid-assisted embrittlement and ductile deformation in the granitoid crust, *Tectonophysics*, *693*, 66–84, https://doi.org/10.1016/j.tecto.2016.10.022.

Wehrens, P., R. Baumberger, A. Berger, and M. Herwegh (2017), How is strain localized in a meta-granitoid, mid-crustal basement section? Spatial distribution of deformation in the central Aar massif (Switzerland), *Journal of Structural Geology*, *94*, 47–67, https://doi.org/10.1016/j.jsg.2016.11.004.

Wilson, R. C. L., G. Manatschal, and S. Wise (2001), Rifting along non-volcanic passive margins: stratigraphic and seismic evidence from the Mesozoic successions of the Alps and western Iberia, *Geological Society Special Publication*, *187*(1), 429–452, https://doi.org/10.1144/gsl.sp.2001.187.01.21.

Wolff, R., K. Hölzer, R. Hetzel, I. Dunkl, and A. A. Anczkiewicz (2024), Late-orogenic extension ceases with waning plate convergence: The case of the Simplon normal fault (Swiss Alps), *Journal of Structural Geology*, *179*(105049), 105,049, https://doi.org/10.1016/j.jsg.2024.105049.

Yin, A. (2006), Cenozoic tectonic evolution of the Himalayan orogen as constrained by along-strike variation of structural geometry, exhumation history, and foreland sedimentation, *Earth-Science Reviews*, *76*(1-2), 1–131, https://doi.org/10.1016/j.earscirev.2005.05.004.

Ziegler, H. J., and A. Isler (2013), Lötschberg-Basistunnel: zusammenfassender geologischer Schlussbericht, *Tech. rep.*, Bundesamt für Landestopografie swisstopo.